High-Throughput Particle Tracking in an Optofluidic Chip

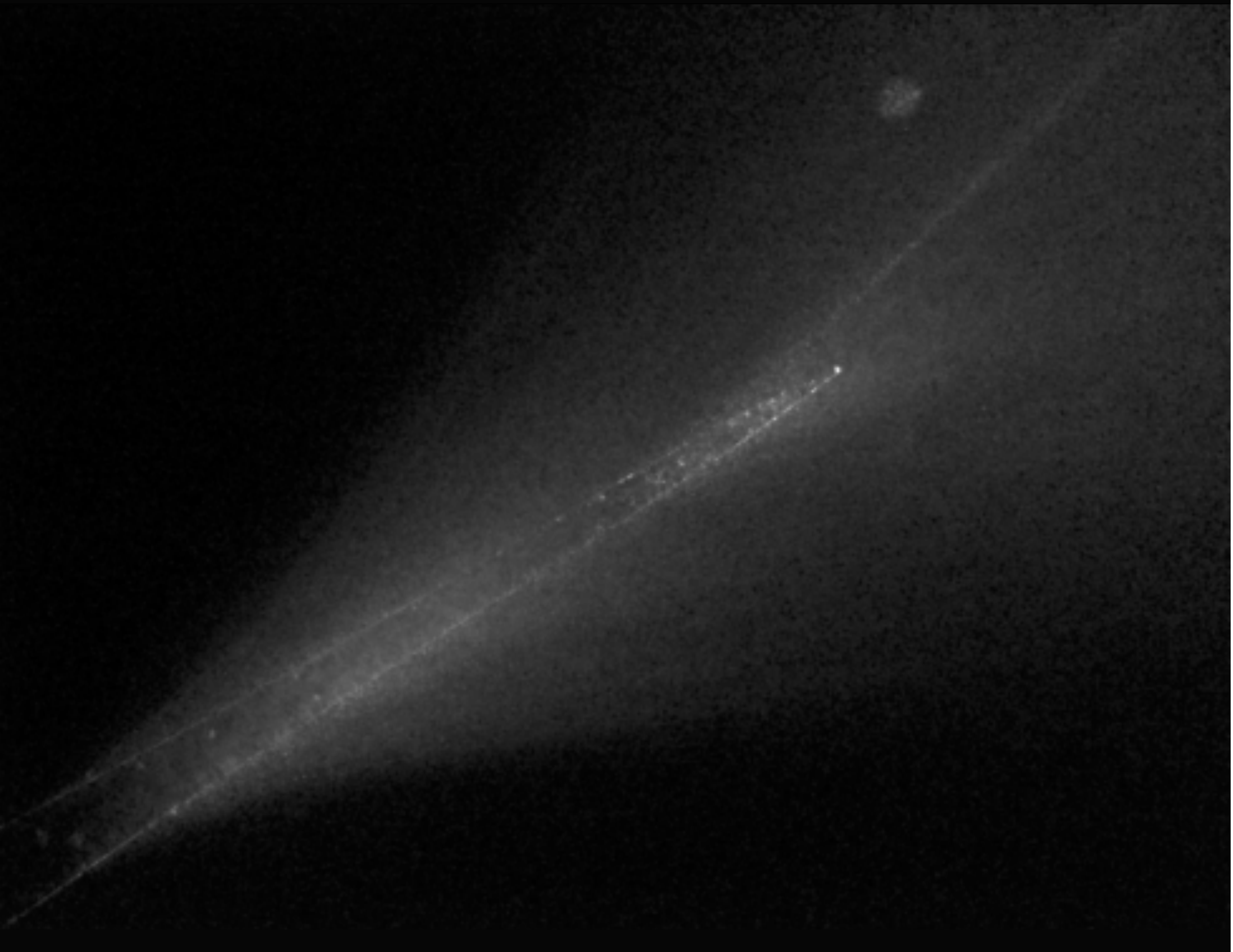

Elena Kyprianou

Faculty of Science

Debye Institute for Nanomaterials Science

Nanophotonics group

High-Throughput Particle Tracking in an Optofluidic Chip

Elena Kyprianou

January 2024

Supervisor: Dr. ir. Sanli Faez

Second examiner: Prof. Dr. Allard Mosk

Abstract

High-throughput and fast particle-tracking techniques are required for the efficient characterization of biological molecules and viruses. The fast detection and characterization of viruses can contribute to the monitoring of disease progress and the development of diagnosis approaches. Here, we present a high-throughput particle tracking technique based on elastic light scattering. We use an optofluidic chip with a micro-sized fluidic channel where the particles are contained. The particles perform Brownian motion and by tracking their position we can study their motion and characterize the particle ensemble. The unique feature of the optofluidic chip is a tapered optical fiber placed on-chip and used to illuminate the particles in the fluidic channel. With our system, it was possible to track the position of thousands of particles with a diameter of 0.3 µm, for durations of a few seconds. Moreover, the scattering microscopy is combined with fluorescence microscopy enabling the potential simultaneous scattering and fluorescence measurements. The combination of scattering and fluorescence microscopy will allow the complete characterization of an ensemble of particles and the determination of the particle type.

Contents

Chapter 1

Introduction

Particle tracking is a widely used method to study particle dynamics. During the last decades, numerous advances in the field of particle tracking have been observed [1, 2]. One of the most used methods for particle tracking has been fluorescence microscopy. However, the limited measurement speed and measurement time of fluorescence-based methods render the tracking of small and quickly diffusing particles difficult, since fast detection and long measurement times are required. The limitations of fluorescence microscopy led to the development of label-free techniques that exploit elastic light scattering to detect and track particles [3–5].

Label-free particle tracking has applications in the fields of biology and medicine. High-throughput and label-free particle tracking techniques are required to efficiently study biological molecules (BMs) and viruses. Particle tracking provides information about the motion of BMs or viruses in their native environment. Analysis of the motion can give the size and concentration of BMs and viruses leading to the complete characterization of an ensemble. This information can contribute significantly to the development of disease diagnostic tools and potentially therapeutic methods for different diseases [6]. Additionally, particle tracking can help to study the effectiveness of drug and gene delivery [7].

An already existing technique that enables the fast, label-free tracking of nanoparticles and viruses uses a single-mode optical fiber with a nanofluidic channel within its core (Figure 1.1) [8]. Using this approach it was possible to track 20 nm-size dielectric particles and 26 nm-size virions. The achieved measurement rates exceeded 3 kHz and the measurement duration was tens of seconds. Based on this approach a commercial setup was created by Dispertech company*, named nanoCET (nanoCapillary Electrophoretic Tracking). The nanoCET setup combines elastic light scattering with fluorescence microscopy. The scattering signal from the particles is detected by a camera, and then the tracking of particles is possible. Fluorescence detection is achieved using an avalanche photodiode (APD) which receives a signal when a particle passes through the field of view (FOV) of the system. A drawback of this approach is that allows the tracking of only a few particles simultaneously. For the accurate characterization of an ensemble of particles, high-throughput methods are needed to obtain statistically significant results.

In this project, our main goal was to increase the throughput of the nanoCET setup to detect and track a larger number of particles simultaneously. To achieve that we had to make some modifications to the initial configuration. The first modification we had to make was to replace the nanofluidic optical fiber with an optofluidic chip. The optofluidic chip has a micro-sized fluidic channel resulting in a larger available volume for the particles. The second modification was to design and fabricate a sample holder compatible with the design of our optofluidic chip and the nanoCET setup. Additionally, we had to replace the objective lens of the microscope with another objective with a larger focal length, to decrease the magnification of the system and thus increase the FOV. The large FOV is important because we want to observe a large ensemble of particles simultaneously. Finally, we needed to replace the APD in the fluorescence part of the setup, with a camera to be able to image the particles within

---

*Dispertech: `https://dispertech.com/home`

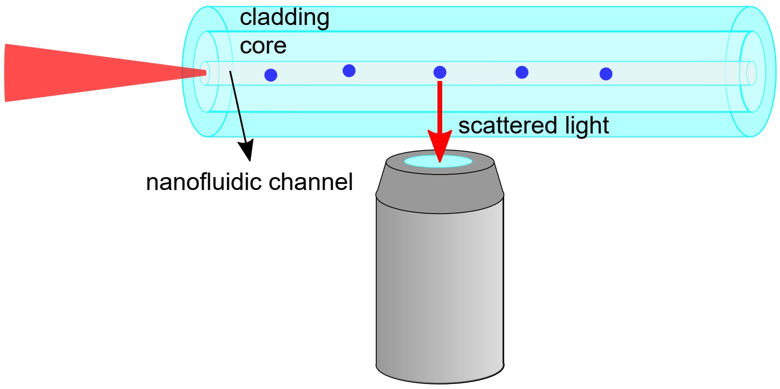

Figure 1.1: Nanofluidic optical fiber. Diagram of the single-mode nanofluidic optical fiber of the nanoCET setup. A nano-sized fluidic channel is within the core of the fiber. A laser beam is coupled into the fiber core and the light scattered by the particles in the channel is collected by an objective lens.

the FOV. Our final configuration has two key features: (1) the illumination and detection in scattering microscopy are orthogonal enabling their efficient separation and thus, achieving a high signal-to-noise ratio, and (2) the use of a tapered optical fiber for the illumination of the particles within the fluidic channel of the chip.

1.1. Thesis outline

We start in chapter 2 with the theoretical background by explaining the most important physics principles related to this project. Afterward, chapter 3 presents the methodology used for the experiments and the data analysis. The topics discussed include the experimental setup, the fabrication of the optofluidic chip, and the analysis approach. In chapter 4, the working principle of the fiber-pulling process is explained, and the results from the characterization of the tapered fibers are shown. Then, chapter 5 presents the scattering microscopy results including the determination of the illumination area, the investigation to find the ideal particle solution concentration, the particle tracking results, and the analysis of the mean squared displacement. Chapter 6 provides the results of particle tracking using fluorescence microscopy, and a comparison with the scattering microscopy. Finally, chapter 7 summarizes the results of this project and provides the conclusions.

Chapter 2

Theoretical Background

This chapter provides an insight into the main theoretical concepts related to this project. Initially, the concepts of Brownian motion, elastic light scattering, and fluorescence are explained. Then, particle tracking is discussed with references to the most widely used particle tracking techniques and multiple-particle tracking. Also, an overview of the field of optofluidics is given. The use of optical fibers as waveguides is explained. Moreover, some basic concepts of microscopy including the depth of focus and magnification follow. Finally, a brief overview of the most common types of noise in optical experiments is given.

2.1. Brownian motion

Brownian motion is the random motion of very small particles which are suspended in a liquid or gas. The medium molecules while performing their thermal motion collide with the small particles resulting in fluctuations in their position. The first who understood this phenomenon was Robert Brown who studied the thermal motion of pollen grains under his microscope in 1827. In 1905, Albert Einstein derived the relation between the diffusive Brownian motion of particles and the thermal energy of the solvent molecules that causes it. For a spherical particle the diffusion coefficient D is given by the Stokes-Einstein relation:

$$D = \frac{k_\mathrm{B} T}{6\pi\eta a} \tag{2.1}$$

where k_B is the Boltzmann constant, T the temperature, η the viscosity of the solvent, and a the hydrodynamic radius.

The diffusive motion of particles is linear with time as Einstein showed in his paper about Brownian motion [9]. The solution of the diffusion equation in 3 dimensions,

$$\frac{\partial n(\mathbf{r}, t)}{\partial t} = D \nabla^2 n(\mathbf{r}, t) \tag{2.2}$$

is given by:

$$n(\mathbf{r}, t) = \frac{e^{-r^2/4Dt}}{(4\pi D t)^{3/2}} \tag{2.3}$$

Using the solution of the diffusion equation the mean squared displacement of particle position can be calculated as follows,

$$\langle r^2 \rangle = \int_0^\infty r^2 n(\mathbf{r}, t) 4\pi r^2 dr = 6Dt \tag{2.4}$$

with n the normalized general solution given in eq.(2.3).

Here, we are interested in the particle motion in two dimensions. The mean squared displacement in 2D is given by,

$$\langle r^2 \rangle = 4Dt \tag{2.5}$$

In this project, we are going to use nanoparticles (NPs) suspended in water. The motion that the NPs perform after their insertion into the microchannel when no external forces act on them, is diffusive Brownian motion.

2.2. Elastic light scattering

Elastic light scattering refers to the scattering of light where the kinetic energy is conserved. When elastic scattering occurs, the wavelength of the scattered light remains the same as the wavelength of the incident light. The two main types of elastic light scattering are Rayleigh and Mie scattering.

2.2.1. Rayleigh scattering

Rayleigh scattering is the elastic scattering of electromagnetic radiation, such as light, by particles. This type of scattering is defined as light scattering by particles that are much smaller than the wavelength of the incident light. The particles behave like point dipoles and the electric field of the wave that the oscillating dipole emits is given by,

$$\mathbf{E}_\mathrm{s} = -\alpha \frac{k^2}{4\pi\epsilon_\mathrm{m} r} \left[\hat{\mathbf{r}} \times (\hat{\mathbf{r}} \times \mathbf{E}_0)\right] e^{ikr - i\omega t} \tag{2.6}$$

where α is the particle polarizability, k the wavevector, r the distance from the particle at which the electric field of the wave radiated by the dipole is evaluated, $\hat{\mathbf{r}}$ a unit vector in the direction of detection, and $\mathbf{E}_0 e^{ikr-i\omega t}$ the electric field of the incident beam [10].

The intensity of the scattered light is $I_\mathrm{s} \sim |\mathbf{E}_\mathrm{s}|^2$, and for unpolarized incident light is given by the following relation,

$$\begin{aligned} I_\mathrm{s} &= I_0 \frac{k^4}{32\pi^2\epsilon_\mathrm{m}^2 r^2} |\alpha|^2 \left(1 + \cos^2\theta\right) \\ &= I_0 \frac{9\pi^2}{2\lambda^4 r^2} \left|\frac{m^2 - 1}{m^2 + 1}\right|^2 V_\mathrm{p}^2 (1 + \cos^2\theta) \end{aligned} \tag{2.7}$$

where I_0 is the intensity of the incident light, and θ the scattering angle [11].

The polarizability of a particle is given by,

$$\begin{aligned} \alpha &= 3\epsilon_\mathrm{m} \frac{\epsilon_\mathrm{p} - \epsilon_\mathrm{m}}{\epsilon_\mathrm{p} + 2\epsilon_\mathrm{m}} V_\mathrm{p} \\ &= 3\epsilon_\mathrm{m} \frac{m^2 - 1}{m^2 + 2} V_\mathrm{p} \end{aligned} \tag{2.8}$$

with $m = \sqrt{\frac{\epsilon_\mathrm{p}}{\epsilon_\mathrm{m}}} = \frac{n_\mathrm{p}}{n_\mathrm{m}}$, where ϵ_p is the particle permittivity, ϵ_m the medium permittivity, n_p the refractive index of the particle, n_m the refractive index of the medium, and V_p the particle volume [11].

Equation (2.7) shows that the scattered light intensity is proportional to the inverse fourth power of the wavelength of the incident light. Thus, the scattering is stronger at short wavelengths. Additionally, the intensity of the scattered light is proportional to the square of the particle volume and hence to the sixth power of the particle size. This results in a weak scattering signal from small particles which is difficult to be detected in experiments.

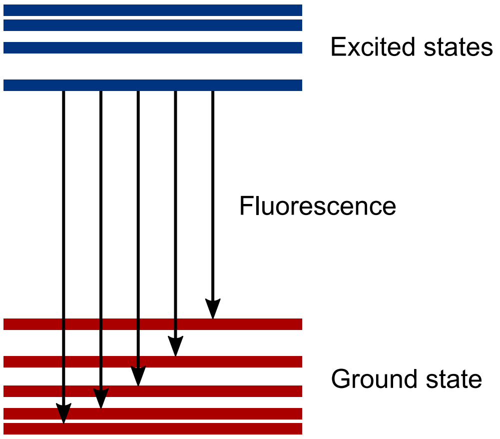

Figure 2.1: Diagram of the fluorescence process. Electrons are excited to a higher-energy state leaving holes in the ground state. Then, the electrons relax to the lowest-energy excited state. After the relaxation, electron-hole recombination takes place by emitting a photon.

2.2.2. Mie theory

When the size of the particles is comparable with the wavelength of the incident light, every volume element of a particle behaves like an oscillating dipole. The incident field on each volume element of a particle is the superposition of the primary beam with the fields radiated by the other dipoles. For most types of particles is complicated to find an exact solution for the field of the scattered light. For spherical particles, the complete Maxwell equations can be solved exactly, and the solution is in the form of an infinite series. This case is called Mie theory.

For the cases where it is more complicated to solve exactly the Maxwell equations, we can make approximations. One approximation is the Rayleigh-Gans-Debye theory. The incident field on every volume element is approximated by the field of the primary beam and the fields coming from the other dipoles are neglected. [11]

2.3. Fluorescence

Fluorescence is defined as the emission of light following the absorption of light with a shorter wavelength. Figure 2.1 shows a diagram of the fluorescence process for a molecular emitter. When light with energy equal to or larger than the energy gap is absorbed by a molecule, excitation of electrons from the ground state to higher-energy states occurs. Excitation of electrons leaves holes in the ground state. Then, the electrons relax to the lowest available excited state through interactions with phonons. Finally, electrons recombine with holes in the ground state by emitting photons with energy equal to the energy gap [12].

2.4. Particle tracking

Particle tracking refers to the observation of the motion of individual particles by repeatedly measuring their position. The most widely used methods for particle tracking are fluorescence and scattering microscopies. One of the challenges of particle tracking is the high measurement speed required to track quickly diffusing particles since the particles diffuse rapidly out of the focal plane. Another challenge is the long observation time necessary to achieve good statistics on the particle motion.

2.4.1. Fluorescence microscopy

Fluorescence microscopy has been the most common method for particle detection and tracking at the nanoscale for decades. High signal-to-background ratios and high spatial resolution render fluorescence microscopy an attractive technique for particle imaging and tracking [1]. However, fluorescence microscopy has also some limitations including (1) limited measurement time due to photobleaching and thermal diffusion, (2) limited measurement speed arising from the low fluorescence emission rate, (3) photoblinking, and (4) the need for labeling that may alter the target properties or introduce interpretation artifacts [4]. These limitations of fluorescence microscopy led to the development of label-free methods for particle tracking experiments.

2.4.2. Elastic light scattering microscopy

A label-free method for particle tracking that overcomes most of the limitations of fluorescence microscopy is elastic light scattering microscopy. One of the advantages of this method compared to fluorescence microscopy is the high measurement speed because the elastic light scattering process is instantaneous and the energy is conserved [8]. One difficulty in detecting scattering signals is that the scattered light intensity is proportional to the square of the particle volume. This makes the detection of nanoparticles difficult because the background scattering dominates over the scattering signal from the particles. However, if the background scattering is constant, it can be subtracted. Scattering-based detection configurations include dark-field scattering microscopy (Figure 2.2(a)) and interferometric scattering microscopy (iSCAT) (Figure 2.2(b)).

In dark-field scattering microscopy, the illumination light and the scattered light are separated such that only the light scattered from the sample contributes to the image formation. A commonly used method to separate the illumination from the scattering is total internal reflection. When the illumination beam travels from a medium with a high refractive index to a medium with a lower refractive index, the beam is reflected at the interface between the two media if the incidence angle is larger than a critical angle. The sample is illuminated by the evanescent field in the lower-refractive index medium. Single biological nanoparticles (BNPs) were detected using nanofluidic scattering microscopy with a dark-field configuration [3]. The BNPs were confined in a nanochannel and the scattered light from the particles was detected. The detection of the BNPs was possible by subtracting the scattering signal of an empty nanochannel from the scattering signal of the nanochannel with a biomolecule in it. Another dark-field scattering microscopy configuration is the orthogonal arrangement of the illumination and detection. This arrangement enables the efficient separation of the illumination light and the light scattered from the sample, providing high signal-to-noise ratios. Nanoparticles with a diameter of 20 nm and virus particles were tracked at a high speed for long durations using a dark-field orthogonal configuration [8].

Another scattering-based method for particle detection and tracking is iSCAT. The principal idea of iSCAT is the interference of a reference beam with light scattered from the sample [4]. Gold NPs with a diameter of 2 nm at a water/glass interface were detected and tracked using iSCAT [13]. Furthermore, iSCAT enabled the 3D tracking of gold NPs on a live cell membrane with microsecond temporal resolution and nanometer spatial resolution [14].

2.4.3. Multiple-particle tracking

Various practical applications require the study of an ensemble of particles rather than single particles. For those cases, it is necessary to detect and track simultaneously multiple particles. Therefore, the development of systems with high throughput and single-particle resolution is

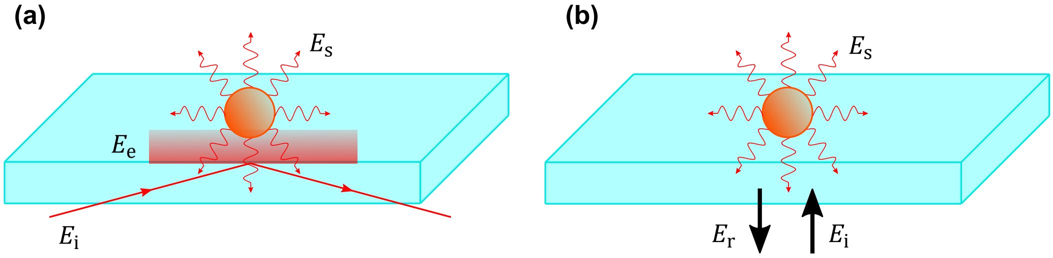

Figure 2.2: Scattering microscopy configurations. (a) Dark-field scattering microscopy. The incident beam (E_i) is reflected by total internal reflection at the glass/air interface and the evanescent field (E_e) illuminates the particle. The particle then scatters light (E_s) that is detected. **(b)** Interferometric scattering microscopy. The incident beam illuminates the particle and a portion of the light is reflected (E_r) at the glass slide. The detected signal is the interference of the reflected beam and the light scattered by the particle.

necessary. Fiber-assisted nanoparticle tracking analysis (FaNTA) is an approach that enables the confinement of nanoparticles in a micro- or nano-sized channel integrated into an optical fiber. This approach has the advantage of high-intensity illumination of the particles within the channel. Additionally, for channels with diameters of a few tens of micrometers, it is possible to study hundreds of nanoparticles simultaneously. An example of such a system is a hollow-core optical fiber with a large-diameter (31 μm) core. Using this system it was possible to image hundreds of 40 nm gold nanospheres simultaneously and then analyze their motion [5]. Another system that enhances, even more, the performance of FaNTA is a single-antiresonant-channel fiber. The effective single-mode guidance allowed by this system enabled the tracking of nanoparticles over more than 1000 frames. Moreover, the precise size determination of monodisperse nanoparticles and the discrimination of two individual particle types with mean diameters 100 nm and 125 nm was possible using the single-antiresonant-channel fiber [15].

One application of multiple-particle tracking is the study of red blood cells (RBCs) to gain information about hematologic diseases [6]. High cell throughput is necessary to properly characterize the RBC population in a blood volume. Simultaneously is critical to have single-cell resolution since hematologic diseases can originate at the single-cell level. Another application is the evaluation of the effectiveness of drug and gene delivery to target cells [7]. With multiple-particle tracking is possible to study the motion of drug and gene carriers in different biological environments. This can give information about the interactions of the carriers with the environment and the carrier delivery rates leading to the development of more effective delivery systems.

In this project, we want to track the position of multiple particles simultaneously using scattering microscopy in a dark-field configuration. Additionally, we are going to combine scattering microscopy with fluorescence microscopy to detect fluorescence signal from the particles within the channel of the optofluidic chip. One example where researchers exploit the advantages of the combination of iSCAT with fluorescence microscopy is tracking the position and orientation of a single virus [16]. Fluorescent quantum dots were attached to virus-like particles and both were tracked using fluorescence microscopy and iSCAT, respectively. The realization of a combined scattering and fluorescence microscope can be made easily by adding a dichroic mirror to separate the scattering wavelength from the fluorescence excitation and emission wavelengths. A detailed protocol with the most important aspects to consider is presented in [17].

2.5. Optofluidics

The field of optofluidics combines microfluidics and optics on the same chip. Microfluidics enables the manipulation of small volumes of fluids, from attoliters to nanoliters, confined in micro-sized channels. Some of the advantages of fluids compared to solids include the possibility to alter the optical properties of the medium in a microfluidic device by replacing the fluid with another fluid, the optically smooth interface between two immiscible fluids, and the formation of gradients in optical properties when miscible fluids mix [18]. There are various examples of applications that exploit the advantages of fluids, such as the oil-immersion objective lens of a microscope and the liquid-crystal displays.

An optofluidic device typically consists of three main parts: (1) a bottom layer where the optics are placed, (2) a middle layer with the microfluidic channels, and (3) a top layer with components to control the microfluidic flow. Examples of developed optofluidic devices include optofluidic microflow cytometers [19], lensless on-chip optofluidic microscopes [20], and optofluidic distributed feedback (DFB) lasers [21].

A structure used for three-dimensional tracking of Brownian motion is a Fabry-Perot microcavity consisting of optical fibers and a microfluidic channel [22]. A single-mode and a multi-mode fiber are inserted in a glass ferrule. A microcavity is formed between the end facets of the two fibers, and the facets are covered with dielectric mirrors. Perpendicular to the glass ferrule at the position of the cavity standing wave, a direct-laser-written structure forms the microfluidic channel which transverses the microcavity (Figure 2.3).

Fluorescence microscopy has also been combined with microfluidics [23] to exploit some of the advantages that microfluidic devices offer. Microfluidic devices enable automatic sample scanning and provide high throughput, characteristics that can be beneficial for fluorescence microscopy imaging.

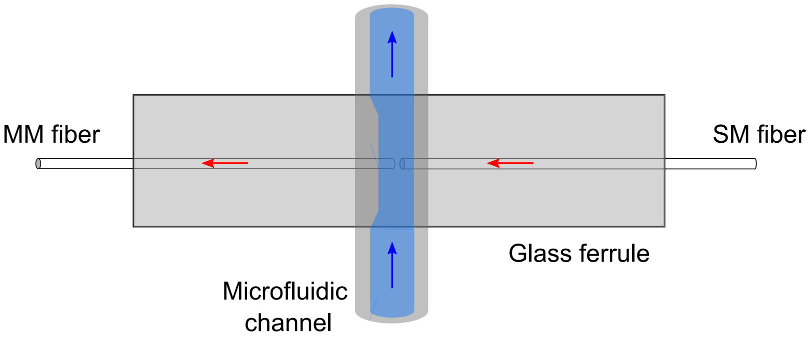

Figure 2.3: Diagram of the Fabry-Perot microcavity. Top view of the microfluidic cavity. The single-mode (SM) and multi-mode (MM) optical fibers are inserted into the glass ferrule forming a cavity between their end facets. The structure for the microfluidic channel is created using a direct writing laser setup. [22]

2.6. Optical fibers

Optical fibers are one of the most reliable ways of light guiding. They typically consist of a core made of a material with a high refractive index and a cladding made of a material with a lower refractive index than the core material. The physical principle underlying the light guiding in an optical fiber is total internal reflection at the core/cladding interface. When a light beam propagates inside the fiber core, it is totally reflected at the core/cladding interface when the incident angle is larger than a critical angle. In this way, the light beam is confined in the core and the optical fiber can guide the beam over long distances. The critical angle for TIR θ_c is given by,

$$\theta_c = \arcsin\left(n_{\text{cladding}}/n_{\text{core}}\right) \tag{2.9}$$

where n_{cladding} is the cladding refractive index, and n_{core} the core refractive index.

There are two main types of optical fibers: (1) the single-mode (SM), and (2) the multi-mode (MM). The SM optical fiber typically has a small-radius core and only one mode can propagate inside its core. In contrast, many different modes can propagate inside the core of an MM fiber [24]. One of the advantages of MM fibers compared to SM is the easy coupling of light in their core. Based on this feature of MM optical fibers, we chose for this project to use an MM fiber to couple in the laser beam and guide the illumination light to the particles.

The numerical aperture (NA) of the MM optical fiber that we use is 0.22, and the focusing lens needs to have an NA smaller or equal to the NA of the fiber for efficient coupling. For this project, we use an aspheric lens with an NA of 0.18 to couple the laser beam into the core of the MM optical fiber.

2.7. Basic concepts of microscopy

2.7.1. Depth of focus

The depth of focus (DOF) of a microscope refers to the range of distances along the optical axis over which the sample remains in acceptably sharp focus. This concept is important for our system since we want to be able to image as many particles as possible. Ideally, the thickness of the fluidic channel of the optofluidic chip needs to be equal to or smaller than the DOF of the system. In this way, all the particles of the sample will be in focus resulting in the most effective system.

For this project, the following relation was used to calculate the DOF [25],

$$\text{DOF} = \frac{\lambda}{4n\left(1 - \sqrt{1 - \left(\frac{\text{NA}}{n}\right)^2}\right)} \tag{2.10}$$

where λ is the wavelength of illumination light, n is the refractive index of the medium between the objective lens and the sample, and NA is the numerical aperture of the system. From eq. (2.10) we can see that lower values of NA will give a larger DOF which is the desired case for this project.

Figure 2.4 shows the DOF calculated using eq. (2.10) for different values of NA. The plot makes clear the relation between the DOF and the NA, and we can see that the largest values of the DOF are achieved for NA less than 0.2. For NA values higher than 0.2, the required thickness of a fluidic channel, if we want all the particles of the sample to be in focus, is less than 10 µm which is more challenging to achieve.

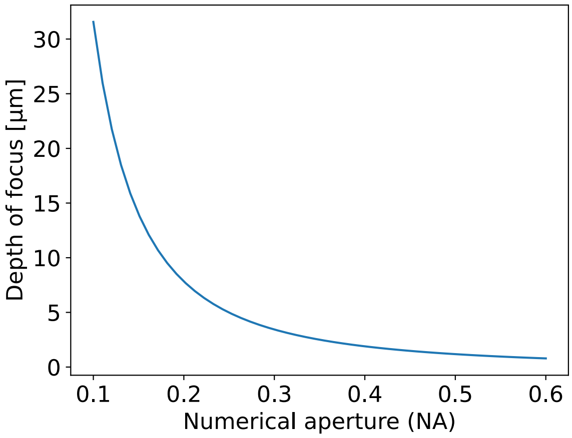

Figure 2.4: Depth of focus. Plot of the DOF for different values of NA (from 0.1 to 0.6). The value of the wavelength was selected to be equal to 633 nm, which is the wavelength of the laser that we use in this project, and the refractive index was set equal to 1.

2.7.2. Magnification

For the calculation of the magnification of the system, two different relations were used. The first involves the distances between the lens and the object and image planes,

$$M = \frac{d_\mathrm{i}}{d_\mathrm{o}} \tag{2.11}$$

where d_i is the distance between the lens and the image, and d_o is the distance between the lens and the object. For the microscope system of this project, d_i corresponds to the focal length of the imaging lens, and d_o to the focal length of the objective lens.

The second relation to calculate the magnification is given by,

$$M = \frac{s_\mathrm{image}}{s_\mathrm{actual}} \tag{2.12}$$

where s_image is the image size, and s_actual is the actual size of the object. For example, if we consider 1 pixel, the image size will be the pixel size as given by the detector specifications, and the actual size will be the real distance that corresponds to 1 pixel (the real distance can be found by calibration of the microscope system, see Appendix A).

The above relations which give the magnification of the system, were combined to calculate the required focal length of the objective lens in order to have a large field of view.

2.8. Noise

In optical experiments, various types of noise can be present. One of them is Poissonian or shot noise which is related to photon detection. The time intervals with which the photoelectrons arrive at the detector follow a Poisson distribution. This type of noise can be approximated by the square root of the number of detected photoelectrons N_det,

$$\sigma_\mathrm{s} = \sqrt{N_\mathrm{det}} \tag{2.13}$$

The number of the detected photoelectrons is given by,

$$N_\mathrm{det} = \mathrm{QE}Nt \tag{2.14}$$

where QE is the detector quantum efficiency, N is the incident number of photoelectrons per second, and t is the exposure time. The only way to reduce the shot noise in measurements is to have a high number of detected photoelectrons.

Another type of noise, which has a technical nature, is the noise related to dark current (electronic shot noise). This is the signal that a detector measures when no light is present and can be calculated by,

$$\sigma_\mathrm{d} = \sqrt{I_\mathrm{d} t} \tag{2.15}$$

where I_d is the dark current which is given by the square root of the number of dark electrons, and t is the exposure time. The electronic shot noise can be subtracted from the measurements if it is known.

Additionally, read noise (σ_r) is always present in a camera. Read noise emerges during the readout process in a camera due to the analog-to-digital conversion and amplification of electrons.

A quantity that can be calculated to give information about the performance of the system, is the signal-to-noise ratio (SNR). SNR can be calculated as the ratio of the number of detected photoelectrons to the noise,

$$\mathrm{SNR} = \frac{N_\mathrm{det}}{\sigma} \tag{2.16}$$

where $\sigma = \sqrt{\sigma_\mathrm{r}^2 + \sigma_\mathrm{d}^2 + \sigma_\mathrm{s}^2}$.

Chapter 3

Methods

In this chapter, the methodology behind this project is explained. Initially, the experimental setup used in this project is presented, and the fabrication procedure of the optofluidic chip is explained. Then, the physical principles behind the process of light propagation in a tapered optical fiber are discussed. Furthermore, the data analysis methods are mentioned, including the background correction and the noise removal approaches used. Finally, the tracking algorithm that we used and its more important features are presented.

3.1. Materials

For the particle tracking measurements using scattering microscopy (chapter 5), we used a solution of polystyrene beads with a mean diameter of 0.3 μm (Sigma Aldrich).

To perform the measurements presented in chapter 6, we used a solution of fluorescent polystyrene beads with a diameter of 0.2 μm.

3.2. Experimental setup

The experimental setup used in this project was initially developed to study the dynamics of particles that move in the nanofluidic channel of a single-mode optical fiber (nanoCET setup) [8, 26]. However, the throughput of the nanofluidic channel is low, and we want to increase it by replacing the optical fiber with an optofluidic chip. Another, modification that we did in the initial setup was to replace the objective lens with another lens with a lower NA and a larger focal length to decrease the magnification and thus increase the FOV of the system (Appendix A, A.1.1). The decrease of the NA resulted also in the increase of the DOF of the system (eq. (2.10)). Additionally, the initial setup had a part for fluorescence microscopy measurements. We modified the fluorescence microscopy part to make it compatible with high-throughput measurements, by adding a lens to illuminate a larger area of the sample. Also, we replaced an avalanche photodiode (APD), which was part of the initial setup, with a camera to be able to image the particles in the sample.

Our experimental setup has two lasers, one with an emission wavelength of 633 nm used for illumination of the particles in the microfluidic channel, and one with an emission wavelength of 488 nm for excitation of the fluorescent particles in the channel. Figure 3.1 illustrates the experimental setup. The beam of the diode laser with λ=633 nm is coupled into an optical fiber, and then a collimating lens creates a collimated beam which is reflected by a mirror towards a beam splitter. The beam splitter splits the beam into two parts: one part is focused by a lens (f=75 mm) on a CMOS camera, and the other part goes to a mirror and then a lens (f=13.86 mm) is used to focus the beam into the core of the multi-mode optical fiber. The mirror before the BS and the lens that focuses the light onto the sample, are located on piezo stages so we can precisely control their positions. The second laser with λ=488 nm is

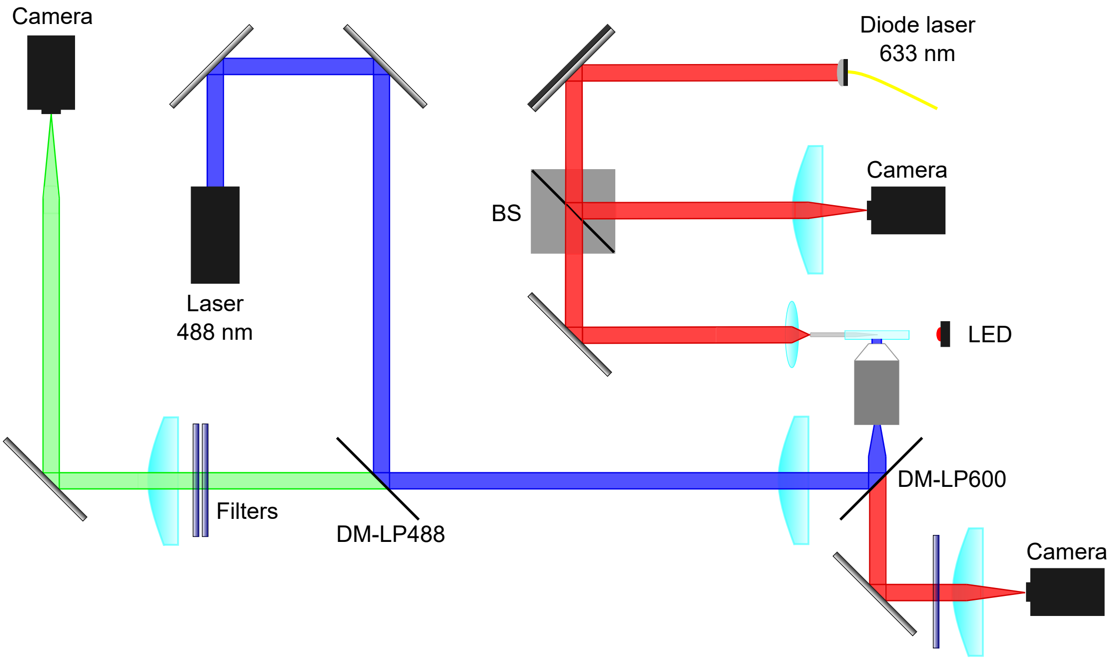

Figure 3.1: Experimental setup. A laser with emission wavelength 633 nm (red) illuminates the particles in the microfluidic channel, and as a result, they scatter light which is detected using a CMOS camera. Another laser with emission wavelength 488 nm (blue) excites the fluorescent particles in the microchannel, and then the fluorescence (green) is detected by another CMOS camera.

used to excite the fluorescent particles in our fluid sample. The laser beam is reflected at two mirrors and then it reaches a dichroic mirror (DM) with a long-pass (LP) filter at 488 nm (DM-LP488). At this DM, the beam is partially reflected to another DM with an LP filter at 600 nm (DM-LP600), so the beam is reflected again. Between the two dichroic mirrors, there is a lens that creates an image plane before the objective lens. Then, the objective lens (f=7.5 mm, NA=0.3) sends a parallel beam of light onto the sample. The purpose of the lens between the two DMs is to create a parallel beam after the objective lens to illuminate a large area of the sample and not a single point.

After the excitation/illumination of the sample, the light emitted from the sample is detected. Both scattered light and fluorescence are collected by the objective lens. Then, the scattered light from the particles in the channel is transmitted by the DM with an LP filter at 600 nm, and a lens (f=100 mm) focuses the beam on a CMOS camera. Before the lens, an LP filter is located which allows only light with a wavelength larger than 500 nm to be transmitted. This filter ensures that only the scattered light from the sample will reach the detector. The fluorescence is reflected by the DM with LP filter at 600nm, and then transmitted by the DM with LP filter at 488 nm. Afterwards, fluorescence passes from two notch filters that block the excitation light so only light due to fluorescence passes through them. A lens (f=100 mm) is used to focus the fluorescence signal onto a CMOS camera (Hamamatsu ORCA-Flash4.0).

Our scattering microscopy setup has two key features that enable long-duration measurements with high signal-to-noise ratios. The first is the orthogonal configuration of the illumination and detection. This configuration results in the efficient separation of illumination and scattering beams leading to high signal-to-noise ratios. The second is the tapered optical fiber that we use for the side illumination of the particles in the fluidic channel. The optical fiber needs to be pulled because we want to create a thin flow channel. The re-

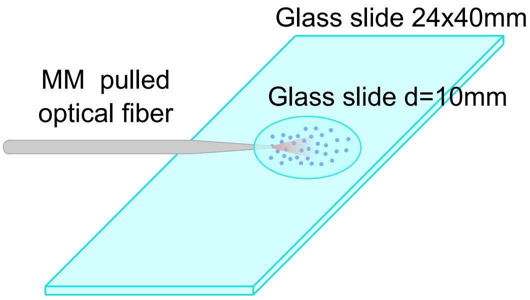

Figure 3.2: Diagram of the optofluidic chip. The bottom layer of the optofluidic chip is a glass slide with dimensions 24 × 40 mm. The middle layer is a multi-mode (MM) pulled optical fiber. The top layer is a circular glass slide with a diameter of 10 mm.

quirement for a thin flow channel arises from the DOF of the system as explained in section 2.7.1.

3.3. Optofluidic chip

The optofluidic chip consists of a bottom glass slide (24 × 40 mm), a multi-mode pulled optical fiber, and a top glass slide (circular with a diameter of 10 mm). The pulled optical fiber has two purposes: (1) it acts as the spacer that forms a fluidic channel between the two glass slides, and (2) it guides the laser beam in the fluidic channel to illuminate the particles.

The first step for the preparation of an optofluidic chip is to clean the glass slides by rinsing them with water, ethanol, isopropanol, and water consecutively. Then the water droplets are blown from the glass slides using nitrogen air. The next step is to place the pulled optical fiber on the bottom glass slide. We want to place the fiber at the correct position every time to have the fiber tip within the FOV during the measurements. For this purpose, we use a 3D-printed mask with the dimensions of the glass slide and a slit at the position where we want to place the fiber (Appendix E). After placing the fiber at the desired position, the mask is removed, and the top glass slide is placed on top of the fiber. To have a thin fluidic channel, it is important to place the top glass slide in such a way that only the pulled part of the optical fiber is within the channel. Finally, to connect the two glass slides a two-component epoxy adhesive glue (Griffon) is used.

For the placement of the optofluidic chip on the experimental setup, we designed and fabricated a sample holder based on the needs of our experimental configuration (Appendix D).

3.4. Light propagation in tapered optical fibers

To illuminate the particles within the fluidic channel of the optofluidic chip, using the tapered optical fiber, it is necessary to couple efficiently the laser beam into the fiber core. To achieve that, we need to make sure that the NA of the fiber matches the NA of the focusing lens used. Then, it is also important to investigate the light propagation into the tapered region of the optical fiber.

The number of guided modes in a tapered optical fiber decreases as the fiber becomes narrower. The propagation of the guided modes can be characterized by the transversal propagation constants k_{t} given by [27],

$$k_{\mathrm{t}}(a) \approx \frac{a_0}{a(z)} k_{\mathrm{t}}(a_0) \tag{3.1}$$

where a_0 is the initial fiber diameter, $a(z)$ is the fiber diameter at a distance z from the fiber tip, and $k_{\mathrm{t}}(a_0)$ is the initial value of the propagation constant for the untapered part of the

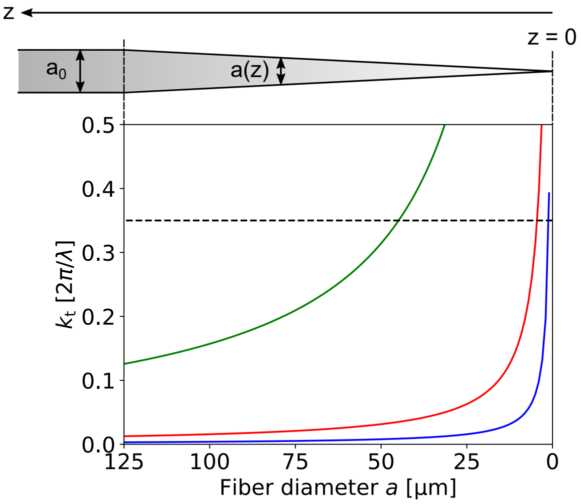

Figure 3.3: Propagation constant evolution. The top part shows a schematic of a tapered optical fiber. The bottom part is a plot of the propagation constant k_t as a function of the fiber diameter. Each line corresponds to a different mode and the dashed line corresponds to the threshold $k_{\mathrm{t,max}}$. [27]

optical fiber. The value of the propagation constant for the tapered regions is larger than the initial value (Figure 3.3).

When a light beam is coupled into an optical fiber, the modes are guided through the whole length of the fiber, and typically they do not escape from the fiber core. In contrast, in a tapered optical fiber, the modes become out-coupled at a specific position within the tapered region. The modes supported by a tapered optical fiber need to fulfill the following condition [27],

$$k_\mathrm{t} < k_{\mathrm{t,max}} = k_0 \mathrm{NA} \tag{3.2}$$

where $k_{\mathrm{t,max}}$ is the maximum allowed value for the fiber to support guided modes, and $k_0 = \frac{2\pi}{\lambda}$ is the wavevector of the propagating light. When a mode does not fulfill this condition is out-coupled. Figure 3.3 shows a plot of the propagation constant as a function of the fiber diameter. The different lines correspond to different modes and the dashed line corresponds to the maximum allowed value of the propagation constant $k_{\mathrm{t,max}}$. The plot shows that modes with larger k_t (green line) become out-coupled at larger taper diameters compared to modes with smaller k_t (blue line) which are out-coupled closer to the fiber tip [27]. Thus, the most efficient tapered fibers are those that have larger $k_{\mathrm{t,max}}$ thresholds and support a higher number of guided modes.

3.5. Analysis

3.5.1. Background correction

When imaging particles, background noise is always present in the recorded images. The sources of the background noise can be scattering due to imperfections or dust on the glass, or scattering from the pulled optical fiber used to illuminate the particles. The background noise can be considered constant if we assume that it is much slower than the particles. Thus, if we know the shape of the background noise we can subtract it from the data.

The approach that we use to find the background noise, is to calculate the median of every pixel over the stack of recorded frames. Then, we approximate the resulting frame with the median values of all the pixels as the background. Finally, we can subtract the background frame from all the frames in the recorded video. In this way, any stationary features in the frames are subtracted and we keep only the moving particles.

3.5.2. Noise removal

For some measurements, it is also useful to subtract the electronic shot noise present in the images. This type of noise arises from the dark signal which is detected by the detector when no light is present.

The electronic shot noise for a single image can be estimated by calculating the variance of pixel values in a dark area of the image. Then, the pixel values that are smaller than the noise level multiplied by a constant value n are set to zero.

3.6. Tracking algorithm

3.6.1. Locating particles

After the background correction and processing of the obtained frames, the next step is to track the position of the particles over time. For this purpose, we use the Trackpy* package. Based on the algorithms of Crocker and Grier [28], Trackpy first locates the particles in each frame, and then it links their positions over time to create their trajectories. The candidate particle locations are found by identifying the local brightness peaks.

To locate the particles in every frame, the algorithm needs two important input parameters. The first is the width of the point spread function (PSF) of particles in pixels (diameter), and the second is the minimum integrated brightness (minimum mass).

The estimation of the PSF can be performed by fitting a 2D Gaussian distribution to the particles in the frames. The function that we use is the following,

$$f(x, y) = Ae^{-B\left[(x-x_0)^2+(y-y_0)^2\right]} + C \tag{3.3}$$

where $A = \frac{1}{2\pi\sigma^2}$, $B = \frac{1}{2\sigma^2}$, and C is a constant offset of the Gaussian distribution which takes into account the background noise present in the data.

For the calculation of the integrated brightness (mass), Trackpy uses the found locally brightest pixel which corresponds to the center of a sphere around a candidate particle. Then, it integrates the brightness of the pixels within the sphere [28]. The minimum mass parameter can take values starting from zero. When it is zero (which is the default value), no filtering is applied and thus the only parameter taken into account to locate particles is the diameter.

3.6.2. Linking particle positions

When the particle positions in every frame of the recorded video are known, the next step is to link their positions over the video to create their trajectories. To do that is necessary to determine which particle in an image corresponds to a particle in the subsequent image. One important quantity that contributes to the identification of the particles is the maximum displacement. The maximum displacement is the larger distance that a particle can travel between two consecutive frames. This distance restricts the area in which the algorithm needs to search to find a particle in the next frame.

3.6.3. Particle dynamics

After locating the particles in the frames and linking their positions it is possible to study their motion. The first to take into account is to subtract any flow present in the recorded video, to observe only the Brownian motion of the particles. To do that Trackpy has a function to calculate the drift. This calculation makes sure that the negative and positive displacements of the particles are equal as expected for particles that perform a random motion.

---

[*] Trackpy: `https://soft-matter.github.io/trackpy/v0.6.1`

The next step is the calculation of the mean squared displacement (MSD). The MSD is given by the following relation [28],

$$\langle r^2 \rangle = \langle |\mathbf{r}(t+\tau) - \mathbf{r}(t)|^2 \rangle \tag{3.4}$$

where $\mathbf{r}(t)$ is the particle position at a time t and $\mathbf{r}(t+\tau)$ is the position of the particle at the time $t+\tau$, with τ the lag time. The MSD is related to the diffusion coefficient according to the eq. (2.5). This relation is useful to extract more information about the investigated particles, such as their size distribution.

Chapter 4

Fiber pulling

This chapter begins with an introduction to the applications of fiber pulling and the purpose of this method in this project. Afterward, the working principle of the fiber-pulling method is explained. Then, the steps needed to be followed to pull an optical fiber are provided. Finally, the results that we obtained from the fiber pulling are presented.

4.1. Introduction to fiber pulling

Tapered optical fibers are widely used for optical sensing applications [29, 30]. They can be used to guide light on a sample and also to collect light. One advantage of tapered optical fibers is the flexibility to illuminate spatially restricted or large areas of a sample [31].

For the light guiding into the microchannel of our optofluidic chip, we use a multi-mode optical fiber. The optical fiber consists of three different layers: (1) an acrylate coating with a diameter of 250 µm, (2) a fluorine-doped silica cladding with a diameter of 125 µm, and (3) a pure silica core with a diameter of 105 µm. However, the diameter of the fiber is larger than the desired thickness of our fluidic channel, so a treatment of the fiber to reduce its diameter is necessary. The method that we use to reduce the fiber diameter is fiber pulling or tapering using a laser-based micropipette puller [32].

4.2. Working principle

The fiber-pulling process involves two crucial steps: (1) heating of the glass, and (2) application of a pulling force. The laser puller uses a CO_2 laser to heat the glass and then a force is applied to pull the fiber and cut it in the middle (Figure 4.1(a)). There are different parameters to control that affect the tip diameter and length. These parameters are heat, filament, velocity, delay, and pull. The heat parameter determines the output power of the laser and typically higher heat values result in longer and finer tips. The filament defines the scanning length of the laser, and the velocity parameter specifies the velocity of the puller bars before the pulling force is applied. The delay parameter controls the time interval between the moment when the laser turns off and the moment when the pulling force is applied. The pulling force is controlled by the pull parameter.

Figure 4.1(b) shows the optical path of the laser beam. The laser beam hits a scanning mirror which is located on a rotating base, and it sends the beam to the back side of the sample. By repeatedly scanning this mirror at a specific scanning interval that is specified by the filament parameter, heat is applied to the sample. There is also another mirror, a concave retro-reflective mirror, located in front of the sample. This mirror, sends the beam of the light that reaches it to the front side of the sample, ensuring the uniform heating of the glass.

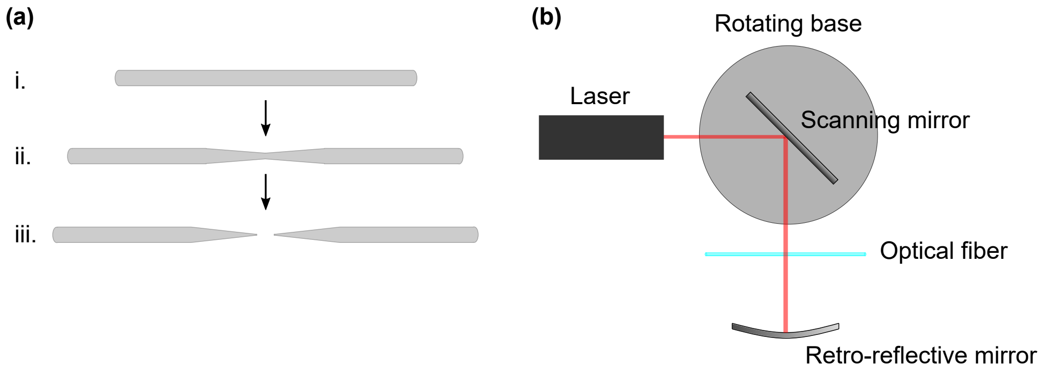

Figure 4.1: Fiber pulling. (a) Fiber pulling steps: A laser heats a fiber with an initial diameter 125 µm (i), and then a pulling force is applied and the fiber becomes thinner at the center (ii) and is also cut into two pieces (iii). **(b)** Optical path of the laser beam (top view). A laser beam is scanned on the back side of the glass by rotating the scanning mirror. Then, the retro-reflective mirror sends the light beam that reaches it to the front side of the sample. In this way, the optical fiber is uniformly heated.

4.3. Fiber pulling steps

The first step before pulling a fiber is the removal of the coating of the multi-mode fibers. This step is necessary to avoid the burning of the coating material. After this step, it is possible to use the laser puller to pull the fiber.

Initially, it is important to let the device warm up for approximately 15 minutes with the lid closed. Then, the fiber needs to be placed in the correct position. This procedure requires to follow a few steps in order to make the pulling possible. The steps are the following:

1. The fiber needs to be placed in the v-groove at the top part of the clamps.
2. The spring stop of the one puller bar has to be depressed and then the clamping knob needs to be tightened.
3. The spring stop of the second puller bar has to be depressed as well, the two puller bars have to be moved toward the central unit, and while the two puller bars are in this position, the second clamping knob has to be tightened.

When the fiber is placed in the correct position, the pulling parameters have to be determined. There are some predefined programs with specific set parameters which can be selected. However, it is also possible to select the desired pulling parameters by selecting one of the available empty programs of the device.

One challenging step of the fiber-pulling process is to place the fiber in the correct position. The fiber without coating is too thin to be clamped properly. For this reason, we used parafilm to hold it at the clamping knob positions. This might affect the reproducibility of the fiber-pulling procedure. One alternative approach that could help to clamp the fiber without affecting the reproducibility of the results is to remove the coating of the fiber only in the part where the fiber would be heated by the laser. In this way, the thickness of the fiber at the positions where it needs to be clamped would be larger and clamping could be possible. For our experiments, we did not choose this approach because after pulling we had to cleave the end of the pulled optical fiber. The cleaving procedure requires to remove the coating from the fiber. However, it was difficult to remove it after pulling due to the short length of the fiber desired for our experiments (3.5 cm). The removal of the coating from a pulled fiber with a length of only a few centimeters would be extremely challenging and the fiber tip could be damaged during this process.

4.4. Fiber pulling results

To find the best combination of pulling parameters, we investigated how different pulling parameters affect the diameter and the length of the fiber tip.

Figure 4.2 shows the images of some fibers pulled using different parameters. The images were obtained using bright-field microscopy. A diagram of the microscope setup used is illustrated in Figure 4.3(a). A white light source illuminates the sample, and then an objective lens (10x/0.25) collects the light coming from the sample. Afterward, the light is focused by a lens on a CMOS camera.

Starting with a set of pulling parameters we got the fiber shown in Figure 4.2(a). The diameter of the fiber tip was calculated at two different positions, indicated by red lines in the images of Figure 4.2. For the fiber in the image 4.2(a), the found diameters are $d_1 \approx 42$ µm and $d_2 \approx 18$ µm. To obtain the fiber in Figure 4.2(c) we increased the heat parameter by 100, so we increased the laser power. This change resulted in a fiber with a thinner and longer tip. The diameters calculated in this case were $d_1 \approx 20$ µm and $d_2 \approx 4$ µm. Finally, we increased the scanning length of the laser beam by increasing the value of the filament parameter. The result was a fiber with even thinner and longer tip as shown in Figure 4.2(e). The calculated diameters for this fiber are $d_1 \approx 13$ µm and $d_2 \approx 3$ µm.

From each pulling attempt, we take two pieces of the same fiber since the fiber during the application of the pulling force becomes thinner and is cut in the middle. The second column of images in Figure 4.2 shows the second piece of each fiber in the first column of images. From the results, we observe that the pulling of the fibers is not always symmetric. If the pulling was symmetric we would expect to have two identical pieces after pulling a fiber. For the fiber of images 4.2(a) and 4.2(b) the pulling seems to be symmetric. The calculated diameters for the fiber in 4.2(b) are $d_1 \approx 42$ µm and $d_2 \approx 17$ µm, which agree with the results for the fiber in image 4.2(a). The asymmetric pulling is more apparent for the fiber in images 4.2(c) and 4.2(d). The calculated diameters for the fiber in image 4.2(d) are $d_1 \approx 22$ µm and

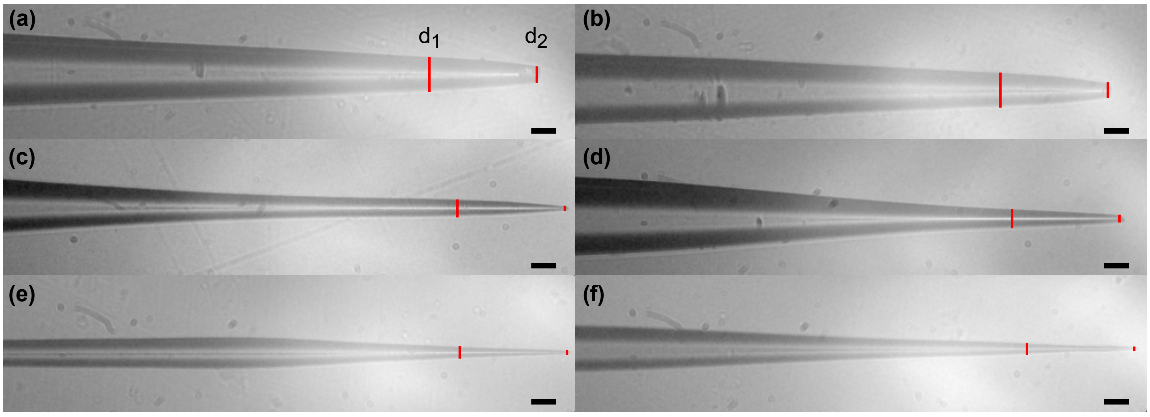

Figure 4.2: Bright-field images of pulled fibers. The optical fibers were pulled using the following parameters: **(a), (b)** Heat=700, Filament=0, Velocity=70, Delay=100, Pull=75. **(c), (d)** Heat=800, Filament=0, Velocity=70, Delay=100, Pull=75. **(e), (f)** Heat=800, Filament=2, Velocity=70, Delay=100, Pull=75. The red lines indicate the distances from the fiber tip end where the diameter of the fiber was calculated. The distance d_1 corresponds to a distance of 140 µm from the fiber tip end, and d_2 to a distance of 2 µm. The scale bar on the images corresponds to 30 µm.

$d_2 \approx 7$ µm. These values are larger than the respective values for the fiber in image 4.2(c). Moreover, it is clearly visible that the tip length is much shorter for the fiber in image 4.2(d). The pulling is not symmetric for the fiber in images 4.2(e) and 4.2(f) as well. The found diameters for the fiber in the image 4.2(f) are $d_1 \approx 12$ µm and $d_2 \approx 3$ µm. These values agree with the diameters of the fiber in image 4.2(e). However, for larger distances from the tip, the two pulled fibers have different shapes and they are not identical.

4.5. Light propagation in pulled optical fibers

After the imaging of the fibers and the calculation of the tip diameter, we investigated the propagation of light through the pulled optical fibers. We used the experimental setup of the Figure 4.3(a) to couple a laser beam into the fiber core. A diode laser passes through a neutral density (ND) filter and then is reflected by two mirrors to reach a lens. The lens is used to focus the laser beam at the fiber end. The fiber is placed on a stage that moves in both the x, y, and z axes so the fiber can be placed at the desired position to achieve efficient coupling of the laser beam into the fiber core. An objective lens collects the scattered light, and then a lens focuses the light onto a CMOS camera.

Images (b)-(e) of Figure 4.3 show some of the pulled optical fibers in air, when the laser beam was coupled into their core. The scattering of light close to the fiber tip is visible in all the images. For the fiber in image 4.3(e), at the tip position we observed interference fringes in contrast to the other fibers. The reason is that the fiber tip was broken resulting in a difference in the path length of the beams reflected at the broken surfaces. The different beams can interfere when their path difference fulfills the conditions for constructive and destructive interference.

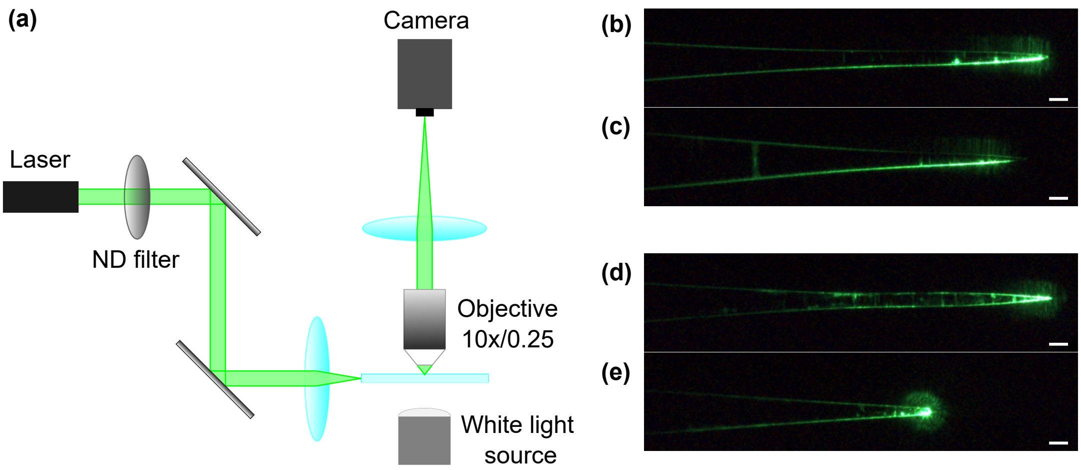

Figure 4.3: Light propagation in pulled fibers. **(a)** Microscope setup used for fiber characterization. This setup was used as a bright-field microscope to image the pulled fibers. A white light source illuminates the fiber and an objective lens collects the light coming from the sample, which is then focused by a lens on a camera. The setup is also used to couple a laser beam in the fiber core. For this purpose, it includes a diode laser, an ND filter to decrease the laser intensity, two mirrors that guide the laser beam to a lens that focuses the beam into the fiber core, an objective lens that collects the scattered light from the sample, and another lens that focuses the light onto a CMOS camera. **(b)-(e)** Images of pulled optical fibers when the laser beam was coupled into their core. The images were taken in air. Images **(b)** and **(c)**, show the two pieces of the same pulled fiber, and images **(d)** and **(e)**, the two pieces of another pulled fiber. The scale bars on the images **(b)-(e)** correspond to 30 µm.

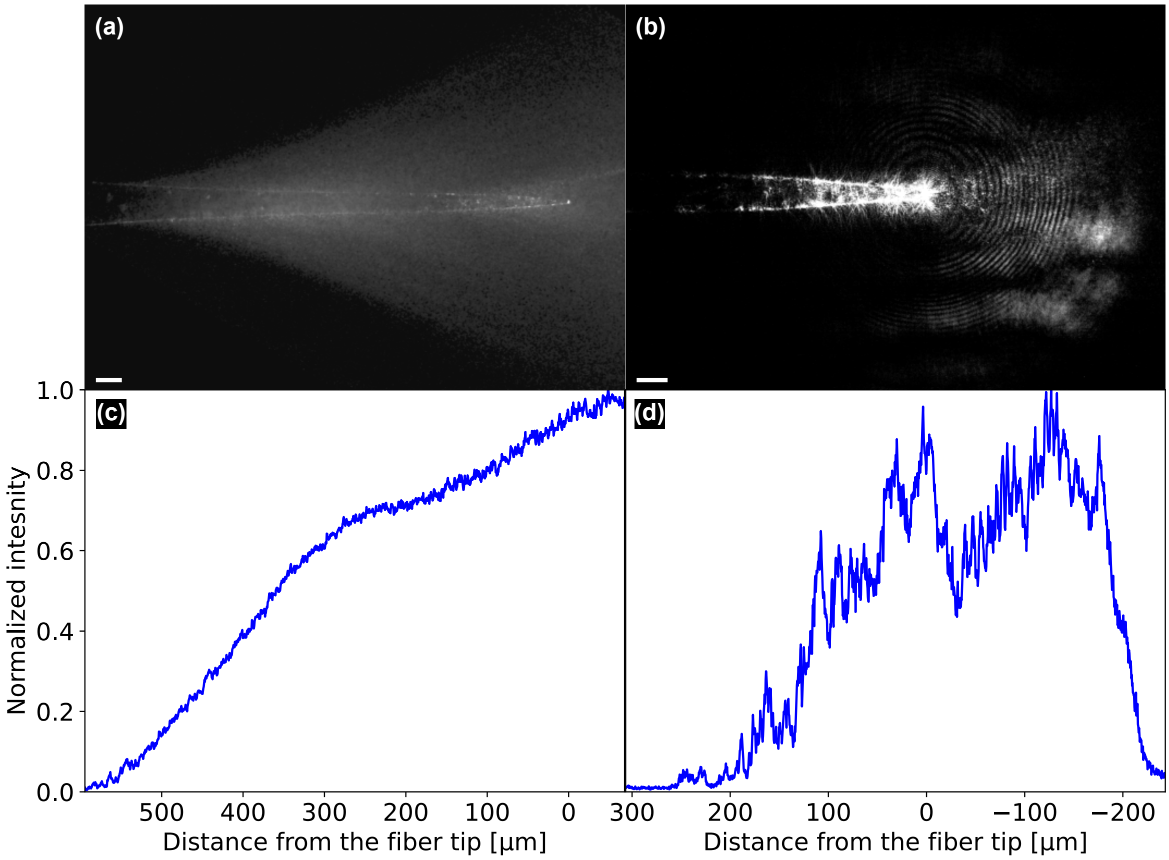

Figure 4.4: Tapered optical fibers in a particle solution. (a) Image of a tapered fiber in a particle solution. The image was recorded using the setup of Figure 4.3(a). **(b)** Image of a tapered optical fiber with a broken tip in a particle solution. This image was recorded using the experimental setup described in section 3.2. The scale bars on both images correspond to 30 µm. **(c)** and **(d)** show the intensity as a function of the distance from the fiber tip for the images **(a)** and **(b)** respectively. The zero value corresponds to the tip position and the negative values to the positions after the fiber output.

We also investigated what happens when the tapered optical fiber is not in air but in a particle solution of polystyrene beads with a diameter of 0.3 µm. Figure 4.4(a) shows an image of a tapered optical fiber in a particle solution and the illuminated area from the light coming out of the fiber. We observe that the light becomes out-coupled at a position that is not close to the fiber tip (≈ 500 µm from the fiber tip). According to section 3.4, this could happen because the $k_{\mathrm{t,max}}$ threshold of the tapered fiber is low and thus the light modes become out-coupled before they reach the fiber tip. Figure 4.4(c) shows a plot of the normalized intensity as a function of the distance from the fiber tip for the image 4.4(a). The intensity increases with decreasing distance from the tip, and it reaches its highest value close to the fiber tip.

Figure 4.4(b) illustrates a tapered optical fiber that had a broken tip, in a particle solution. In contrast to the image 4.4(a) here we do not observe a well-defined illuminated area, but interference fringes. As explained earlier for the fiber image in the air, these fringes arise from the broken fiber tip. The normalized intensity as a function of the distance from the tip is shown in Figure 4.4(d). The trend is the same as before, the intensity increases as the distance from the tip decreases and it peaks close to the fiber tip. In this case, the intensity increase is not smooth, as we observe some fluctuations. After the fiber tip, at the output of the fiber, the peaks that correspond to the interference fringes are visible.

To conclude, the characteristics of the light at the output of the tapered optical fibers can indicate if the fiber is damaged or if it is an efficient waveguide. Hence, after the investigation of the light propagation in the tapered fibers, we can decide which fibers are appropriate for this project to guide the illumination light in the fluidic channel of our optofluidic chip.

Chapter 5

Scattering microscopy results

5.1. Fiber alignment and light coupling into fiber core

To illuminate the particles in the fluidic channel we need first (i) to align the optical fiber, and (ii) to couple the laser beam into the fiber core. For these procedures, we use the part of the experimental setup illustrated in Figure 5.1(a). For the fiber alignment process, we use a red LED which illuminates the optical fiber. The reflected light is focused on a camera, and in this way, we can image the surface of the fiber input in which we want to couple the laser beam. For the light coupling into the fiber core, we use a diode laser with a wavelength of 633 nm coupled into an optical fiber. First, the laser beam hits a mirror that is placed on a piezo stage. Then, the beam is transmitted from a beam splitter and hits another mirror which reflects it on a lens. The lens is also placed on a piezo stage and is used to focus the laser beam into the fiber core. The piezo stage of the lens allows us to match the position of the fiber input with the focal point of the lens, which is a requirement for efficient light coupling into a fiber.

Some representative results from the fiber alignment and light coupling procedures are presented in Figure 5.1(b). In images 5.1(b)(i), 5.1(b)(iii), and 5.1(b)(v) we can see the surface of the fiber end. The fiber end was cleaved before the fiber alignment process. The surface of the fiber end in the image 5.1(b)(i) seems damaged. The reason can be that the cleaving was not performed properly or is also possible that the fiber end was damaged during handling. The cleaving is not perfect for the fiber end in the image 5.1(b)(iii) as well. In image 5.1(b)(v)

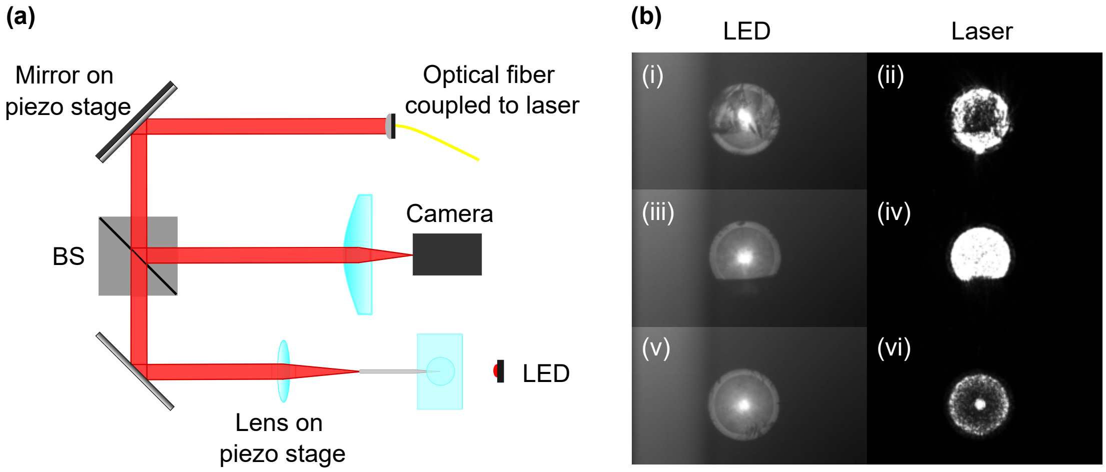

Figure 5.1: (a) Diagram of the part of the experimental setup used to perform the fiber alignment and light coupling procedures. **(b)** Results from the fiber alignment and light coupling. Images (i), (iii), and (v) show the surface of the fiber end from the fiber alignment procedure using the LED. Images (ii), (iv), and (vi) show the laser spot.

the fiber end is properly cleaved.

Images 5.1(b)(ii), 5.1(b)(iv), and 5.1(b)(vi) show the laser spot. For the fiber in image 5.1(b)(ii) it was difficult to couple the laser beam properly, probably due to the damaged surface. In the image 5.1(b)(iv) we can see the light coupled into the fiber core, however, is not clear if the laser beam is coupled only into the core or if it also penetrates the cladding. In this case, a lower exposure time or lower laser power could give us a better image. However, it was not possible to reduce them further, as we had already used the lower values allowed by our system. Finally, in the image 5.1(b)(vi) we can see a small, bright spot at the center of the core which is the laser beam, coupled in the fiber core.

5.2. Determination of illumination area

After coupling the laser beam into the core of the tapered multi-mode optical fiber, the light coming out of the fiber is divergent and creates an illumination cone inside the fluidic channel of the optofluidic chip. To estimate the area of illumination within the FOV of our system, we performed scattering microscopy measurements using a dense solution of polystyrene beads with a diameter of 0.3 µm. The dilution of the particle solution used is 300× in deionized water.

Figure 5.2 shows an image of the illuminated area within the FOV. The background scattering and the electronic shot noise were subtracted from the image using the approaches explained in 3.5.1 and in 3.5.2, respectively. The calculated area of illumination is 0.13 mm^2. To find the volume of illumination, we need to estimate the channel thickness. For this measurement, a long part of the fiber was inside the fluidic channel, not only the tapered part. Hence, the maximum channel thickness is 125 µm which is the cladding diameter. However, the channel thickness is not necessarily uniform and it could be smaller for the part of the channel where the tapered part of the fiber was located. So in this case is challenging to determine the minimum channel thickness. Considering the maximum channel thickness, the maximum illumination volume is 0.016 µL.

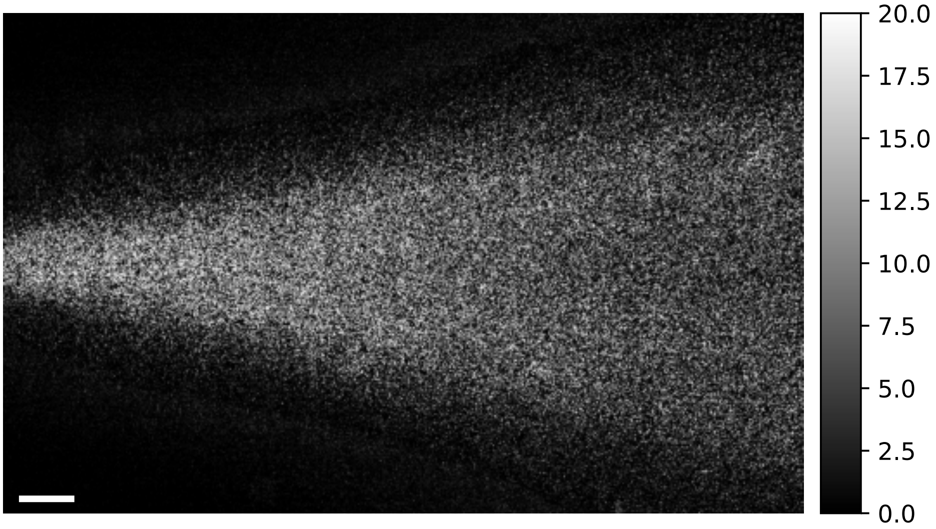

Figure 5.2: Image of illumination area within the FOV. The estimated illumination area is 0.13 mm^2. The channel thickness maximum limit is 125 µm resulting in a maximum illumination volume of 0.016 µL. The scale bar on the image corresponds to 50 µm.

5.3. Concentration investigation

The ideal concentration of the particle solution is the one that enables us to distinguish individual particles in the images. To find this concentration, we performed scattering microscopy measurements using different dilutions of the particle solution. Figure 5.3 shows scattering images for different dilutions. The background scattering in the obtained images was subtracted using the approach discussed in 3.5.1.

The image 5.3(a) shows the scattering obtained using a dilution of 4000×. This dilution is high to be able to distinguish individual particles because there is much scattering from the large number of particles in the fluidic channel. For image 5.3(b) the dilution is 6000×, and the particles start to be distinguishable. In image 5.3(c) the dilution is 8000×, and similar to image 5.3(b) it is possible to observe a few individual particles. However, there are still some areas in the image where it is not easy to distinguish the particles. Finally, image 5.3(d) shows the scattering from particles in a 10000× diluted solution. In this case, it is possible to observe individual particles and thus track their position over time.

For each image, a different optofluidic chip was used to perform the measurements. This could also affect the results as the tapered optical fibers used in every sample are not identical and thus the channel thickness is not exactly the same.

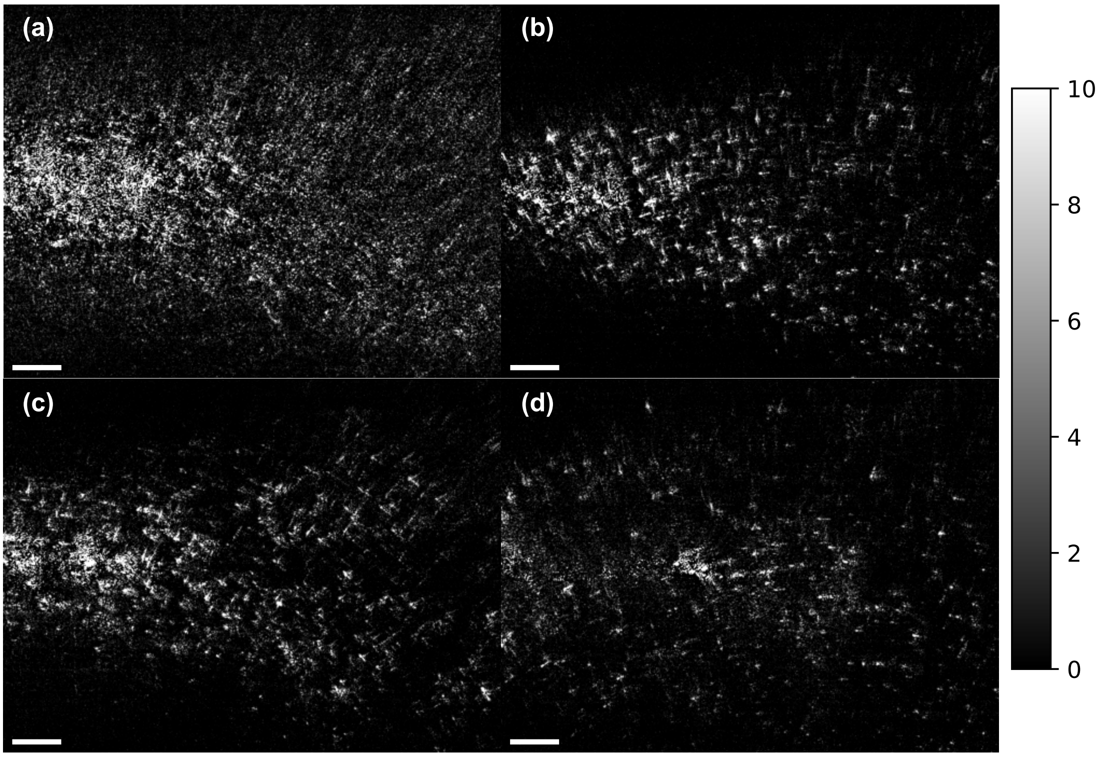

Figure 5.3: Concentration investigation. The images show the obtained scattering images for different dilutions of the particle solution in deionized water. The dilutions studied are: **(a)** 4000×, **(b)** 6000×, **(c)** 8000×, and **(d)** 10000×. The position of the fiber used to illuminate the particles in the images is at the left side of the images at the middle of the image height. The fiber contributes a constant background scattering which was subtracted. The fibers used for every sample are not identical so the thickness of the channels varies. The estimated channel thicknesses for every image are: **(a)** 20-70 µm, **(b)** 20-45 µm, **(c)** 20-45 µm, and **(d)** 20-50 µm. The scale bar in all the images corresponds to 30 µm.

5.4. Particle tracking using scattering microscopy

After finding the ideal particle solution concentration, we performed scattering measurements over time. To track the position of the particles in the fluidic channel of the optofluidic chip we need first to locate the particles in every frame. Then, we can link the particle positions to create the trajectory of each particle. To locate the particles we use the *locate* function of Trackpy. This function needs as input parameters the diameter of the particles and the minimum mass, as discussed in 3.6.1.

5.4.1. Estimation of input parameters for tracking algorithm

Particle size determination

The particle diameter was estimated by fitting a 2D Gaussian distribution to the particles as explained in 3.6.1. After the 2D Gaussian fitting, the full width at half maximum (FWHM) of the Gaussian distribution was calculated for each particle to estimate the point spread function (PSF) size. The resulting PSF size is 5.0 ± 0.2 pixels. This size was used as an input parameter for the tracking algorithm to locate the particles in the video. Figure 5.4 shows an example of the fitting process for a particle. The image of a particle and the corresponding 2D fitted Gaussian distribution is illustrated in Figure 5.4(a). Figure 5.4(b) shows the cross-cuts of the fitted distribution over the x position.

Threshold determination

The next step is the estimation of the minimum integrated brightness or mass (section 3.6.1) that we need to use to detect the particles in every frame and avoid the false detection of noise. To estimate this threshold, we counted the detected features over 100 frames of a video for different values of the minimum mass. Figure 5.5 shows a plot of the number of detected features as a function of the minimum mass parameter. The highest value of mass in the investigated frames is between 35 and 40 as Figure 5.5 shows. For values larger than the maximum value, we do not expect to detect any features in the frames. This is in agreement

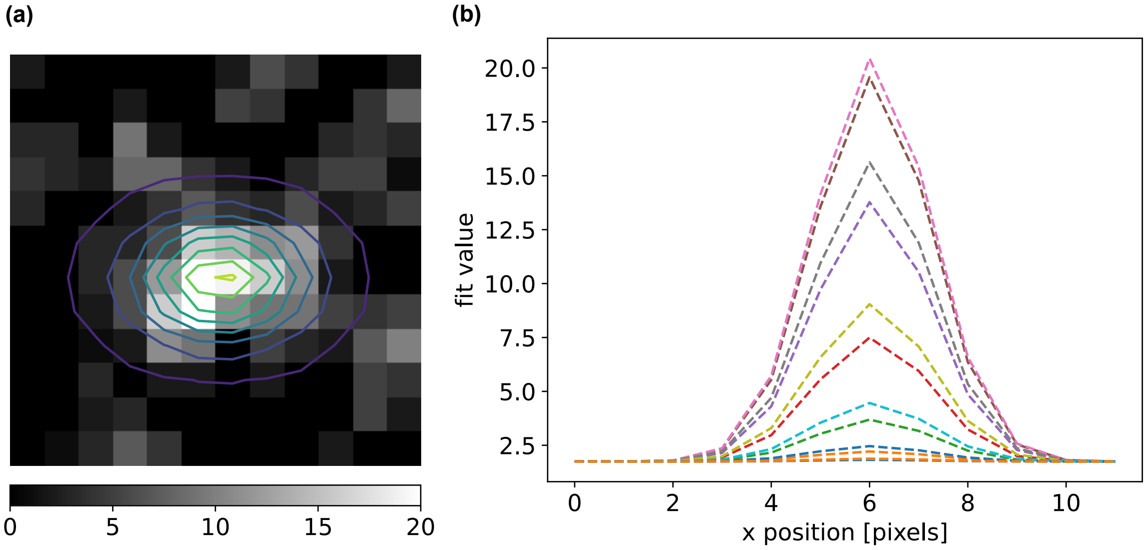

Figure 5.4: 2D Gaussian fitting. (a) Image of a particle in a frame. The point spread function (PSF) of the particle was fitted with a 2D Gaussian distribution. The contour lines correspond to the fitting. **(b)** Cross-cuts over the x position. Every cross-cut corresponds to a different row of pixels in the image.

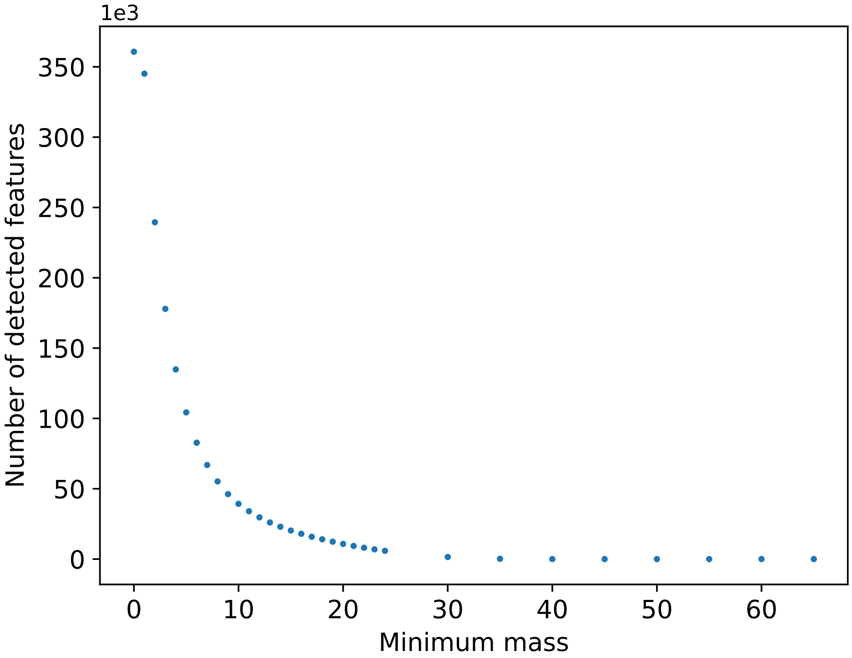

Figure 5.5: Threshold determination. The plot shows the number of detected features over 100 frames as a function of the minimum mass. The number of detected features increases with decreasing minimum mass.

with the results in Figure 5.5. When the minimum mass parameter takes values lower than the maximum mass, the algorithm starts to detect features in the video. The number of detected features increases with decreasing minimum mass. When the value of the minimum mass approaches really small values (<5), the number of detected features shows a significant increase. In this limit, the detected features correspond also to noise in the frames and not only to particles. The value that we selected to use as the minimum mass for the tracking algorithm is 8.

5.4.2. Particle tracking results

After determining the particle diameter and the threshold that we need to use as input parameters for the tracking algorithm, it was possible to locate the particles in every frame and then link their positions to study their behavior over time.

To locate the particles in every frame of the recorded video, the input parameters used for the tracking algorithm are the diameter and the threshold that we estimated (section 5.4.1). We used a diameter of 5 pixels and a minimum mass of 8. Figure 5.6(a)-(d) shows the found particles in some of the video frames. The particles were located by the algorithm, and then their positions were linked to find their trajectories. Afterward, a filtering step was performed to filter out the particles with short trajectories (shorter than 20 frames). The particles indicated in the images of Figure 5.6 are the particles that survived after the filtering step. From the images, it is clear that the detected features correspond to particles as there are no detected speckle patterns that correspond to noise.

The trajectories of the found particles are illustrated in Figure 5.6(e). These trajectories were obtained after drift subtraction to remove the flow present during the measurements as explained in 3.6.3. Over a video of 1000 frames, 1170 particles were tracked in 2 dimensions. The longest trajectory found has a length of 216 frames which corresponds to approximately 3 seconds.

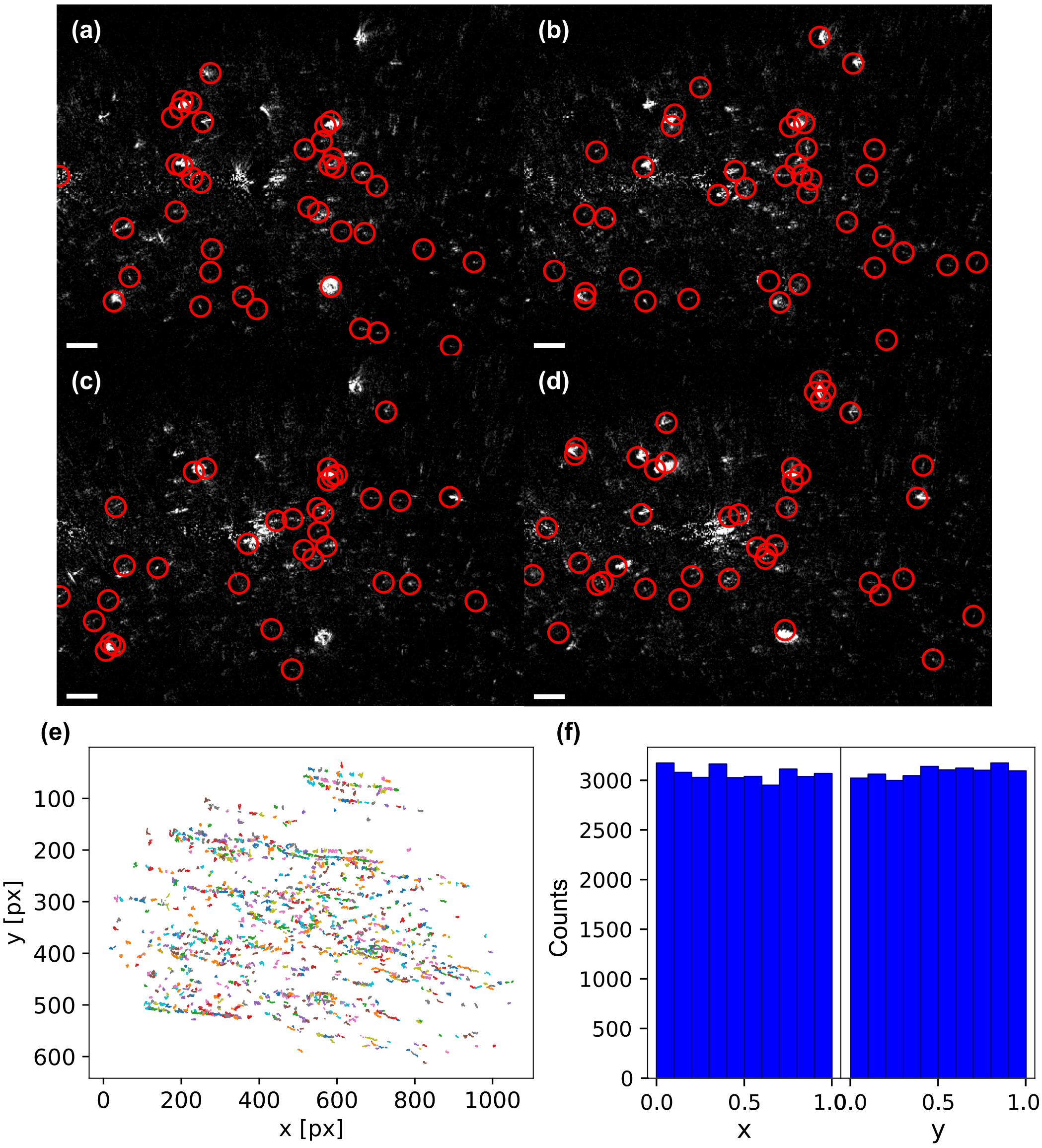

Figure 5.6: Locating particles and particle trajectories. The images **(a)-(d)** show the found particles. The parameters used in the tracking algorithm are diameter=5 pixels and minimum mass=8. The particles indicated in the frames are the particles found to have longer trajectories than 20 frames. The scale bars in the images correspond to 20 µm. **(e)** Plot of the particle trajectories in 2 dimensions. **(f)** Subpixel accuracy investigation. The flat histograms indicate that we do not have pixel bias in our measurements.

Finally, we investigated the subpixel accuracy of our measurements. Figure 5.6(f) shows the resulting histograms for the x and y positions. The fact that the histograms are flat indicates that there is no pixel bias in our measurements.

5.5. Mean squared displacement analysis

The mean squared displacement of every particle in the sample was calculated as a function of time. Figure 5.7(a) shows an example of the MSD curve for a particle. The mean squared displacement increases linearly over time as expected for diffusive Brownian motion. We used eq. (2.5), MSD = $4D\tau$, to perform a linear fit on the experimental data. From the slope of the linear fit, we can extract the diffusion coefficient D. The question that emerges is which is the optimum number of data points to use for the fitting to accurately calculate the diffusion coefficient.

5.5.1. Determination of the optimum number of fitting points

The lag times for every trajectory, are calculated by averaging position differences over the entire trajectory [33]. This results in a higher statistical significance for the shorter lag times compared to the longer ones. Thus, is not the most precise approach to take all the points of the MSD plot into account in the fitting procedure. Only a few points that correspond to short lag times need to be used to have accurate results. To find the optimum number of data points that we need to use, we performed a linear fitting of the MSD of every particle

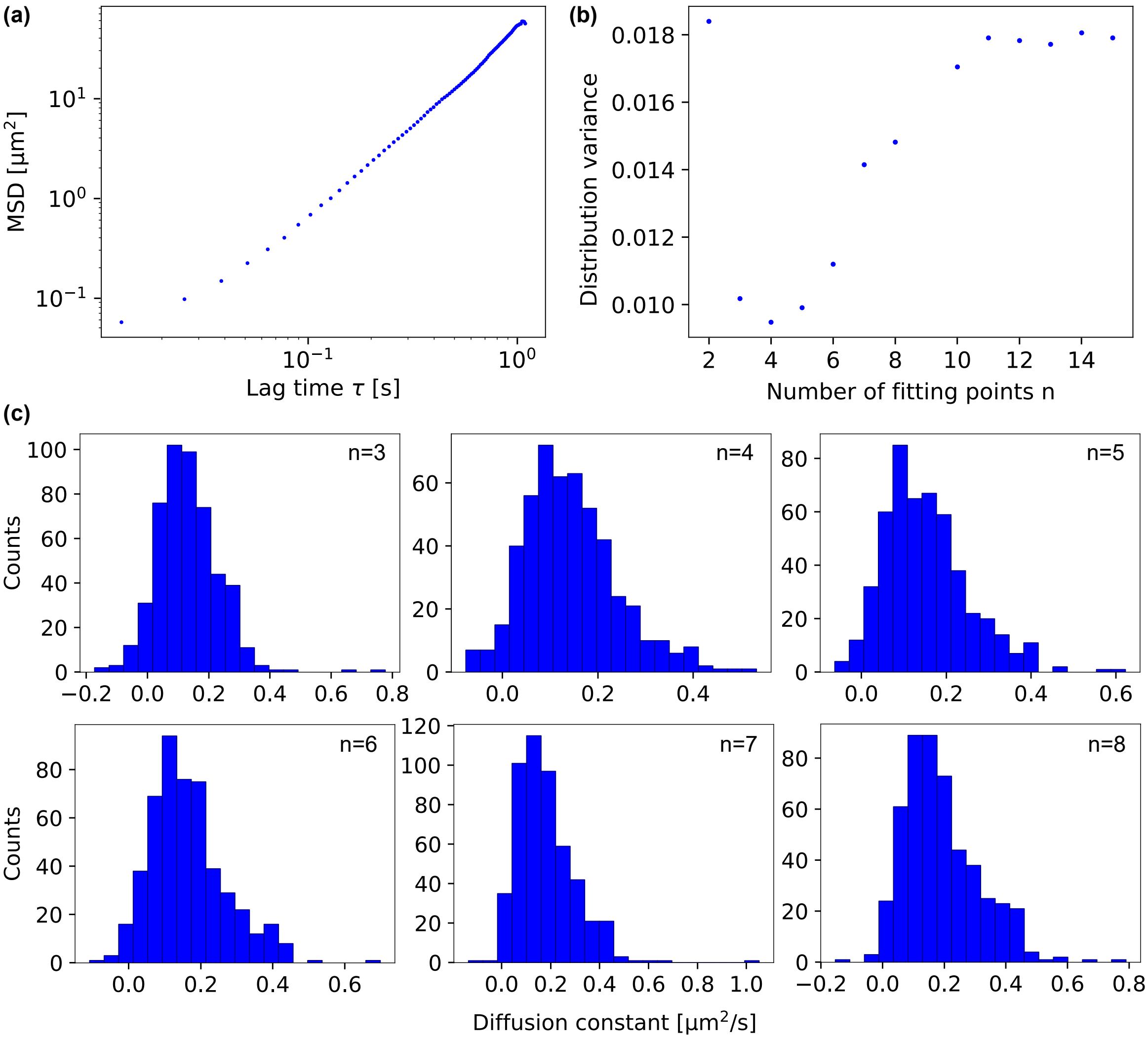

Figure 5.7: MSD analysis. (a) MSD as a function of lag time. The plot shows an example of the MSD of one of the tracked particles. The results are plotted on a logarithmic scale. **(b)** Variance of diffusion coefficient distributions as a function of the number of fitting points. The curve exhibits a minimum at n=4. **(c)** Diffusion coefficient distributions for different numbers of fitting points, n. Each distribution presents the calculated diffusion coefficients of 500 particles for a specific number of data points used to fit the MSD of each particle. From the histograms we observed that there are a few negative values of the D. These values are not physical and they probably correspond to false detections of noise.

using different numbers of data points. For every number of data points, we calculated the diffusion coefficient of each particle and plotted their distributions. Figure 5.7(c) shows the diffusion coefficient distributions for some of the numbers of data points that we fitted. We can observe that the width of the distribution changes for different numbers of fitting points. To determine the optimum number of data points n, we investigated the variance of each histogram. We expect that the narrower distribution is the one that will give us the most accurate result for the diffusion coefficient. Figure 5.7(b) shows the variance of the diffusion coefficient distributions as a function of the number of fitting points. For small numbers of fitting points (n=2 and n=3), we observe a decreasing trend and for n=4 the curve has a minimum. For n > 4, the variance increases and it seems that for n > 11, it approaches a plateau. The narrower distribution corresponds to n=4 where the curve exhibits a minimum. Hence, we conclude that the optimum number of data points to use for the MSD fitting is 4.

5.5.2. Calculation of hydrodynamic diameter

The diffusion coefficient is directly related to the hydrodynamic radius via the Stokes-Einsetin equation (eq.(2.1)). Using the diffusion coefficients found from the MSD fitting with 4 data points, we calculated the hydrodynamic radius of each particle. The distribution of the hydrodynamic diameter is shown in Figure 5.8(a). We plotted only the range of hydrodynamic diameters that correspond to physical values. In the initial distribution, we had also negative values that were not physical and arose from false-detected particles. Additionally, we had a few values much larger than the upper bound of 10 µm that we chose, which do not correspond to the particles of interest as well. The size distribution was fitted with an inverse Gaussian function [34] given by,

$$f(x) = \frac{1}{\sqrt{2\pi}\sigma x^2} e^{-\frac{(1/x-\mu)^2}{2\sigma^2}} \tag{5.1}$$

The inverse Gaussian distribution exhibits a sharp rise at small diameters and a long tail towards larger diameters. The calculated median value of the hydrodynamic diameter is d = 0.19 µm and the standard deviation of the distribution is $\sigma = 0.31$ µm.

A second approach to calculate the hydrodynamic size of the particles is to study the MSD of the ensemble. Figure 5.8(b) shows the MSD of the ensemble of particles as a function

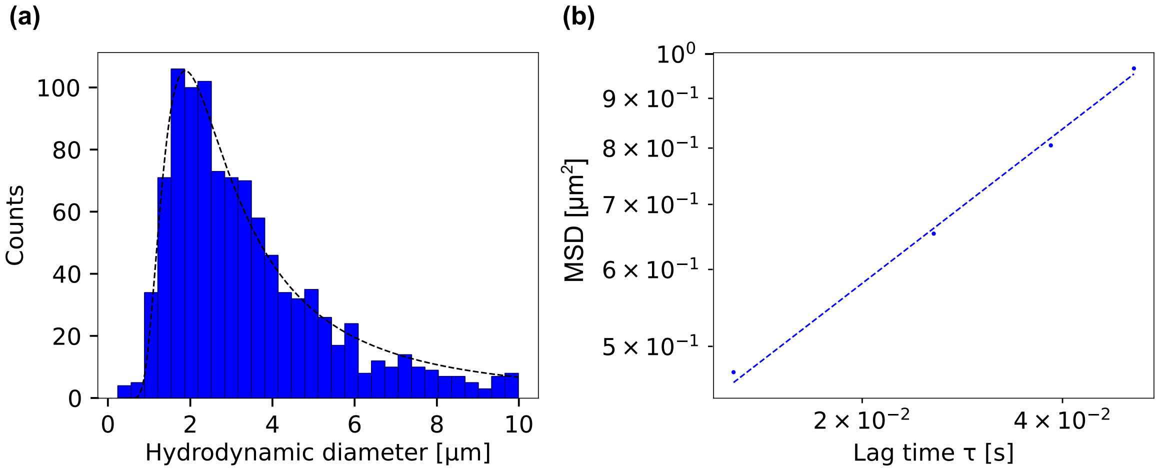

Figure 5.8: Hydrodynamic diameter determination. (a) Distribution of hydrodynamic diameter calculated using the Stokes-Einstein relation. The dashed line represents an inverse Gaussian fitting. **(b)** MSD of the ensemble of particles as a function of the lag time. The MSD was fitted with a linear relation (dashed line).

of lag time. We performed a linear fit using the first 4 data points. The slope of the line is $4\boldsymbol{D}$, and thus it gives us the diffusion coefficient. The result for the diffusion coefficient is $\boldsymbol{D} = 1.14 \pm 0.10$ µm^2/s. Then, we can calculate the hydrodynamic size of the particles using the Stokes-Einstein relation. We found that the hydrodynamic diameter is d = 0.38 ± 0.03 µm.

Chapter 6

Fluorescence microscopy results

6.1. Fluorescence vs scattering imaging

Using fluorescent polystyrene beads with a diameter of 0.2 µm, we performed scattering and fluorescence measurements. Our sample is the optofluidic chip explained in section 3.3. We initially performed scattering measurements by illuminating the particles in the channel through the tapered optical fiber. Afterward, using the same sample, we performed fluorescence measurements by illuminating the particles with a 488 nm laser as explained in section 3.2.

Figure 6.1 shows the results obtained. The found particles in a single image for scattering measurements are indicated in Figure 6.1(a), and for fluorescence measurements in Figure 6.1(b). The indicated particles were found by Trackpy. For the used particle solution concentration (600× dilution in deionized water), the detected particles are less for scattering experiments compared to fluorescence. A possible reason could be that the scattering signal from the particles was weak or we did not have many particles within the FOV.

6.2. Particle tracking using fluorescence microscopy

Using Trackpy, we found the particles in every frame of the recorded video and we linked their positions to create their trajectories. Figure 6.2(a) illustrates the particle trajectories in 2 dimensions. The particle solution concentration that we used allowed us to track 359

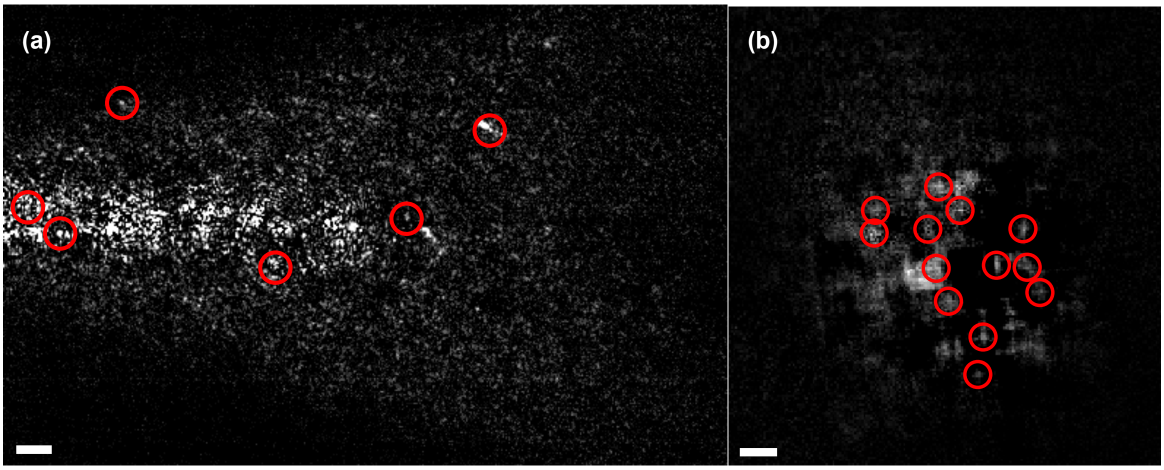

Figure 6.1: Scattering vs fluorescence imaging. (a) Scattering image of fluorescent polystyrene beads with a diameter of 0.2 µm. **(b)** Fluorescent image of the same sample as in **(a)**. The red circles indicate the particles found by Trackpy. These are the particles that survived after filtering out the particles with short trajectories. The scale bar in both images corresponds to 10 µm.

particles using fluorescence microscopy. The longest trajectory that we found is 275 frames which corresponds to approximately 7 seconds. From the scattering measurements that we performed using the same sample, it was possible to track only 43 particles with the longest trajectory corresponding to approximately 1 second.

Additionally, we investigated again the subpixel accuracy of the fluorescence measurements. The histograms of Figure 6.2(b) show the results for the x and y positions. As for the scattering measurements, the histograms are flat and thus we can conclude that there is no pixel bias in our measurements.

6.2.1. Hydrodynamic diameter determination

After particle tracking, we calculated the diffusion coefficient for every tracked particle by performing a linear fitting to the MSD data points. Then, we found the hydrodynamic diameter of each particle using the Stokes-Einstein relation. The distribution of the hydrodynamic diameter is shown in Figure 6.3(a) for the scattering measurements and in Figure 6.3(b) for the fluorescence measurements. The number of the found particles from scattering measurements is low and thus the distribution could not be fitted with a function. The hydrodynamic diameter distribution for the fluorescence measurements was fitted with an inverse Gaussian distribution (eq. (5.1)). The found median hydrodynamic diameter is $d = 0.28$ µm and the standard deviation of the distribution is $\sigma = 0.37$ µm.

The hydrodynamic diameter was also calculated using the ensemble MSD plots illustrated in Figure 6.3(c) and Figure 6.3(d) for the scattering and fluorescence measurements respectively. Using the scattering measurements, we found that the hydrodynamic diameter is $d = 0.23 \pm 0.04$ µm. This result agrees with the known particle diameter for the particles used. The result using the fluorescence measurements is $d = 0.57 \pm 0.01$ µm which is higher than the size provided by the manufacturer by approximately a factor of 3. The median diameter calculated using the hydrodynamic diameter distribution is also slightly higher than the expected value. A possible reason could be the aggregation of many particles resulting in the overestimation of the particle size. Moreover, photobleaching might have occurred, affecting the fluorescence properties and the obtained size distribution.

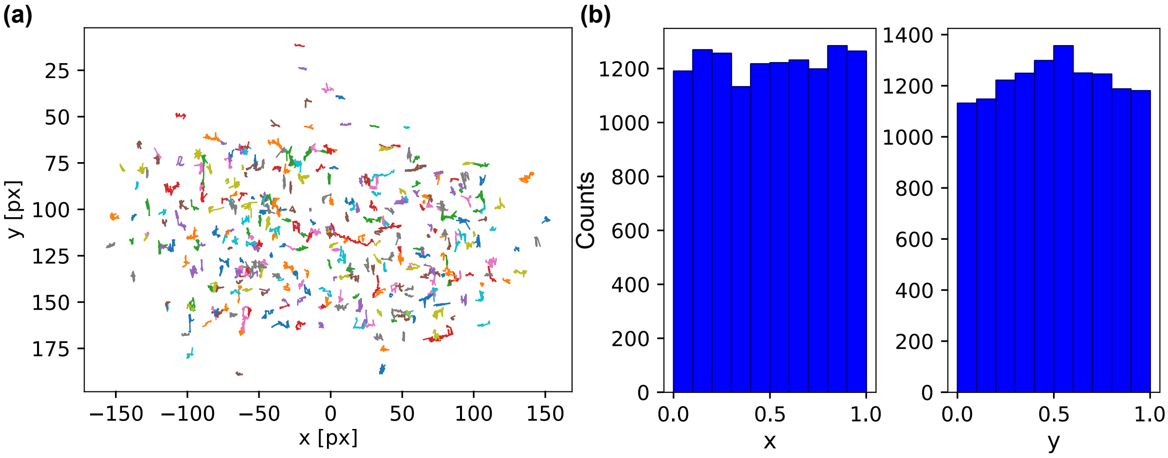

Figure 6.2: Particle tracking results using fluorescence microscopy. (a) Particle trajectories in 2 dimensions. The particles that we tracked are 359. **(b)** Investigation of subpixel accuracy. The flat histograms show that there is no pixel bias in the measurements.

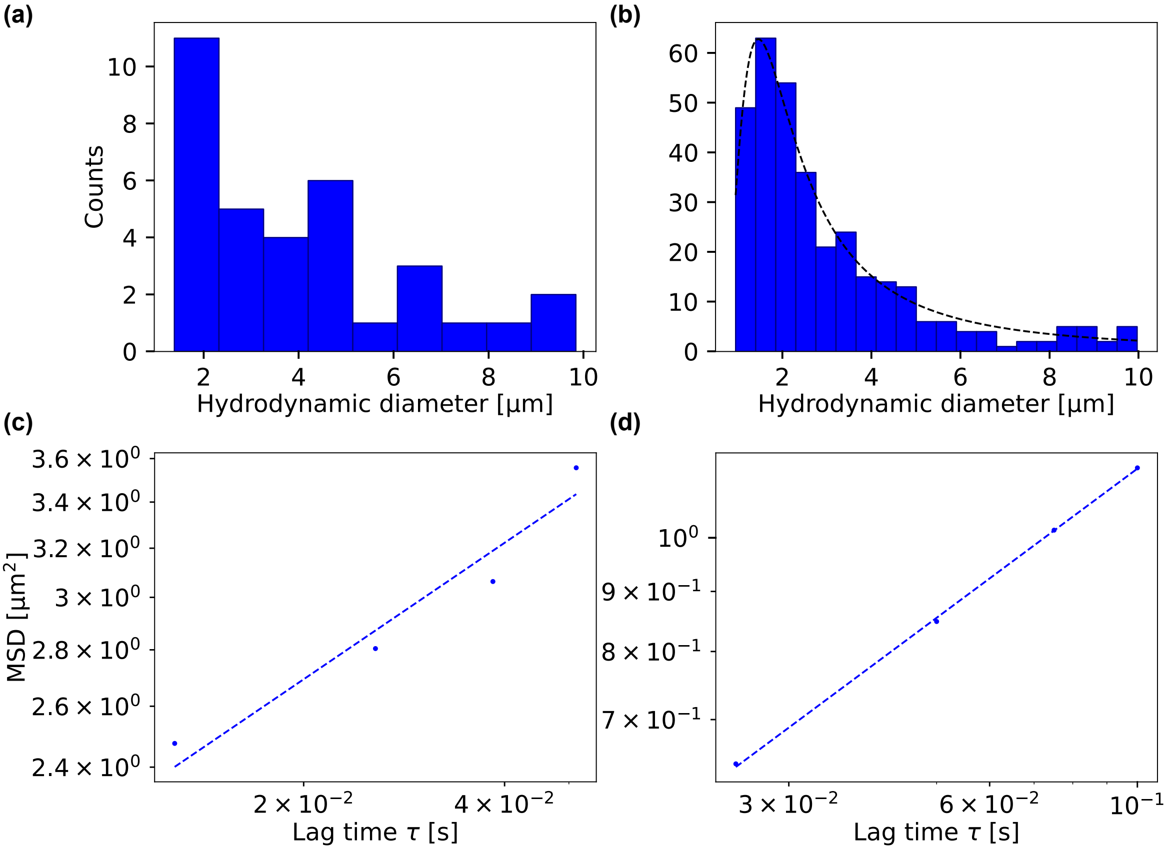

Figure 6.3: Particle size determination using fluorescence and scattering measurements. Hydrodynamic diameter distribution from: **(a)** the scattering measurements, and **(b)** the fluorescence measurements. Mean squared displacement over time, calculated from the scattering measurements (plot **(c)**) and the fluorescence measurements (plot **(d)**).

6.3. Combination of scattering and fluorescence microscopy

Particle tracking using scattering microscopy provides the information needed to characterize the ensemble of particles. However, in the case where we have a mixture of fluorescent and non-fluorescent particles to study, scattering microscopy itself cannot distinguish the different types of particles. For this reason, we tried to combine scattering with fluorescence microscopy. In this way, it will be possible to detect simultaneously scattering and fluorescence signals and thus characterize the particles and distinguish them.

The experimental setup that we used is explained in section 3.2. We tried to perform simultaneous scattering and fluorescence measurements, but the specific configuration of the setup does not allow the matching of the focal planes of the two detectors. Hence, it is not possible to observe simultaneously the particles on both cameras in focus and detect scattering and fluorescence signals at the same time. Further investigation is necessary to be performed to find the appropriate optical elements needed to match the focal planes of the two detectors.

Chapter 7

Conclusion

High-throughput particle tracking techniques can open the way for the development of more efficient disease diagnostic methods and the optimization of drug and gene delivery systems. To contribute to this aim, in this project, we presented a high-throughput, label-free particle tracking approach based on elastic light scattering microscopy. Our system uses an optofluidic chip having a channel with a thickness of a few tens of micrometers. The unique feature of the optofluidic chip is the tapered optical fiber placed on the chip. The tapered fiber guides the illumination light into the fluidic channel where the investigated particles are contained. Using this system, particle tracking of thousands of particles was possible for durations of a few seconds. Moreover, the mean squared displacement of the particles was analyzed to gain information about the particle size distribution.

Elastic light scattering microscopy can provide a complete characterization of a type of particles that perform Brownian motion in the fluidic channel of the chip. However, to distinguish different types of particles in a mixture of particles, it is necessary to obtain more information. The combination of scattering microscopy with fluorescence microscopy can achieve this goal. In this project, we performed some preliminary measurements using a system with combined scattering and fluorescence. The successful combined measurements were not possible due to a focus mismatch of the two detectors of the system. Further investigation is necessary to optimize the combined scattering and fluorescence configuration to perform simultaneous measurements.

There are also some limitations and drawbacks in our system that can be investigated further in future studies. One drawback is the fact that the fluidic channel of the optofluidic chip might have a thickness that is not homogeneous. The reason is that the tapered optical fiber does not always have the same diameter over the whole length that is placed in the channel. A possible solution to this would be to add a coating around the tapered optical fiber. The coating could also increase the strength of the tapered fiber resulting in a more robust and easy-to-handle structure.

Additionally, the effectiveness of the system could be further enhanced by decreasing the fluidic channel thickness to be able to have all the particles in focus. To achieve that, it is necessary to produce thinner and longer fiber tips, something that was challenging to achieve here with the device that we were using for fiber pulling.

Bibliography

1. Manzo, C. & Garcia-Parajo, M. F. A review of progress in single particle tracking: From methods to biophysical insights. *Reports on Progress in Physics* **78** (2015).
2. Ma, Y., Wang, X., Liu, H., Wei, L. & Xiao, L. Recent advances in optical microscopic methods for single-particle tracking in biological samples. *Analytical and Bioanalytical Chemistry* **411,** 4445–4463 (2019).
3. Špačková, B. *et al.* Label-free nanofluidic scattering microscopy of size and mass of single diffusing molecules and nanoparticles. *Nature Methods* **19,** 751–758 (2022).
4. Taylor, R. W. & Sandoghdar, V. Interferometric Scattering Microscopy: Seeing Single Nanoparticles and Molecules via Rayleigh Scattering. *Nano Letters* **19,** 4827–4835 (2019).
5. Förster, R. *et al.* Tracking and Analyzing the Brownian Motion of Nano-objects Inside Hollow Core Fibers. *ACS Sensors* **5,** 879–886 (2020).
6. Guruprasad, P. *et al.* Integrated automated particle tracking microfluidic enables high-throughput cell deformability cytometry for red cell disorders. *American Journal of Hematology* **94,** 189–199 (2019).
7. Suh, J., Dawson, M. & Hanes, J. Real-time multiple-particle tracking : applications to drug and gene delivery. **57,** 63–78 (2005).
8. Faez, S. *et al.* Fast, Label-Free Tracking of Single Viruses and Weakly Scattering Nanoparticles in a Nanofluidic Optical Fiber. *ACS Nano* **9,** 12349–12357 (2015).
9. Einstein, A. Über die von der molekularkinetischen theorie der wärme geforderte bewegung von in ruhenden flüssigkeiten suspendierten teilchen. *Ann. d. Phys.* **322,** 549–560 (1905).
10. Griffiths, D. J. *Introduction to Electrodynamics* (Harlow: Pearson Education Limited, 2014).
11. Imhof, A. Scattering techniques in soft condensed matter. *Soft Condensed Matter Lecture Notes* (2022).
12. Valeur, B. & Berberan-Santos, M. N. *Molecular Fluorescence: Principles and Applications* (John Wiley & Sons, Incorporated, 2013).
13. Holanová, K., Vala, M. & Piliarik, M. Optical imaging and localization of prospective scattering labels smaller than a single protein. *Optics and Laser Technology* **109,** 323–327 (2019).
14. Taylor, R. W. *et al.* Interferometric scattering microscopy reveals microsecond nanoscopic protein motion on a live cell membrane. *Nature Photonics* **13,** 480–487 (2019).
15. Nissen, M. *et al.* Nanoparticle Tracking in Single-Antiresonant-Element Fiber for High-Precision Size Distribution Analysis of Mono- and Polydisperse Samples. *Small* **18** (2022).
16. Kukura, P. *et al.* High-speed nanoscopic tracking of the position and orientation of a single virus. *Nature Methods* **6,** 923–927 (2009).
17. Ortega Arroyo, J., Cole, D. & Kukura, P. Interferometric scattering microscopy and its combination with single-molecule fluorescence imaging. *Nature Protocols* **11,** 617–633 (2016).

18. Psaltis, D., Quake, S. R. & Yang, C. Developing optofluidic technology through the fusion of microfluidics and optics. **442,** 381–386 (2006).
19. Zhang, Y. *et al.* Optofluidic device based microflow cytometers for particle/cell detection: A review. **7,** 1–21 (2016).
20. Cui, X. *et al.* Lensless high-resolution on-chip optofluidic microscopes for Caenorhabditis elegans and cell imaging. *Proceedings of the National Academy of Sciences of the United States of America* **105,** 10670–10675 (2008).
21. Li, Z., Zhang, Z., Emery, T., Scherer, A. & Psaltis, D. Optofluidic distributed feedback dye laser. *Conference on Lasers and Electro-Optics and 2006 Quantum Electronics and Laser Science Conference, CLEO/QELS 2006* **14,** 245–248 (2006).
22. Kohler, L., Mader, M., Kern, C., Wegener, M. & Hunger, D. Tracking Brownian motion in three dimensions and characterization of individual nanoparticles using a fiber-based high-finesse microcavity. *Nature Communications* **12,** 1–7 (2021).
23. Paiè, P., Martínez Vázquez, R., Osellame, R., Bragheri, F. & Bassi, A. Microfluidic Based Optical Microscopes on Chip. *Cytometry Part A* **93,** 987–996 (2018).
24. Fang, Z., Chin, K., Qu, R. & Cai, H. *Fundamentals of Optical Fiber Sensors* (John Wiley & Sons, Incorporated, 2012).
25. Young, I. T. *et al.* Depth-of-Focus in microscopy. *8th Scandinavian Conference on Image Analysis,* 493–498 (1993).
26. Faez, S. *et al.* Nanocapillary electrokinetic tracking for monitoring charge fluctuations on a single nanoparticle. *Faraday Discussions* **193,** 447–458 (2016).
27. Pisanello, M. *et al.* Tailoring light delivery for optogenetics by modal demultiplexing in tapered optical fibers. *Scientific Reports* **8,** 1–11 (2018).
28. Crocker, J. & Grier, D. Methods of Digital Video Microscopy for Colloidal Studies | Elsevier Enhanced Reader. *Journal of Colloid and Interface Science* **179,** 298–310 (1995).
29. Korposh, S., James, S. W., Lee, S. W. & Tatam, R. P. Tapered Optical Fibre Sensors: Current Trends and Future Perspectives. *Sensors (Basel, Switzerland)* **19** (2019).
30. Taha, B. A. *et al.* Comprehensive review tapered optical fiber configurations for sensing application: Trend and challenges. *Biosensors* **11,** 1–20 (2021).
31. Pisanello, F. *et al.* Dynamic illumination of spatially restricted or large brain volumes via a single tapered optical fiber. **20** (2017).
32. P-2000 Laser-Based Micropipette Puller System Operation Manual. *Sutter Instrument Company,* 1–88 (2020).
33. Ernst, D. & Köhler, J. Measuring a diffusion coefficient by single-particle tracking: Statistical analysis of experimental mean squared displacement curves. *Physical Chemistry Chemical Physics* **15,** 845–849 (2013).
34. Kim, J. *et al.* Locally Structured On-Chip Optofluidic Hollow-Core Light Cages for Single Nanoparticle Tracking. *ACS Sensors* **7,** 2951–2959 (2022).

Acknowledgements

Foremost, I would like to express my deepest gratitude to my supervisor, dr. ir. Sanli Faez for his continuous support and encouragement during my master's project. It was a pleasure to work under your guidance and I appreciate all your suggestions and insightful feedback.

I would like to extend my sincere appreciation to the second examiner of my thesis, Prof. Dr. Allard Mosk for his helpful suggestions and advice.

I am also grateful to Dr. Itir Bakiş Dogru Yüksel, Dr. Zhu Zhang, and Anna Peters for their valuable advice, help, and guidance in the lab. Special thanks also to all the technicians of the Nanophotonics group, Dante Killian, Arjan Driessen, Jan Bonne Aans, and Paul Jurrius, for their contributions in solving the technical difficulties emerging in the lab. Thanks also to all the members of the Nanophotonics group for the fruitful discussions.

Special thanks to Dr. Pieter Kooijman, lab manager of Lili's Proto Lab, for his valuable advice and support to 3D print components for my experimental setup.

I also wish to thank Aron Opheij, R&D scientist of Dispertech company, for his guidance in operating the nanoCET setup and software.

I am also extremely grateful to my family and friends for their encouragement and support throughout my master's journey.

Appendix A

Calibration measurements

A.1. nanoCET setup calibration

We performed a calibration of the nanoCET microscope to convert the pixel values in distance, and thus be able to know our field of view (FOV) in distance units (µm).

For the calibration, we used a micro-ruler (Thorlabs R1L3S2P). We placed the micro-ruler on a glass slide on the sample holder of our setup. The illumination source that we used was a white light source in a bright-field configuration.

Figure A.1(a) shows one of the obtained images of the micro-ruler. Using this image, it was possible to calibrate the microscope since we know the distance between the micro-ruler lines. The distance between the large lines of the micro-ruler is 100 µm and the distance between the small lines is 10 µm (Figure A.1(a)). Using ImageJ software, the distance between the large lines was measured in pixels for all the recorded images, and the result was that 718 pixels correspond to 100 µm. Therefore, our calibration gives that 1 pixel corresponds to 0.139 µm.

The FOV of our system is 1920 × 1200 pixels. Using the calibration, the FOV in distance units is 267 µm × 167 µm. This FOV is small for the purposes of this project because we want to perform high-throughput measurements. So, it is important to have a larger FOV to observe more particles simultaneously. For this reason, we replaced the objective lens of the microscope with an objective with a lower magnification, to increase the FOV of the system.

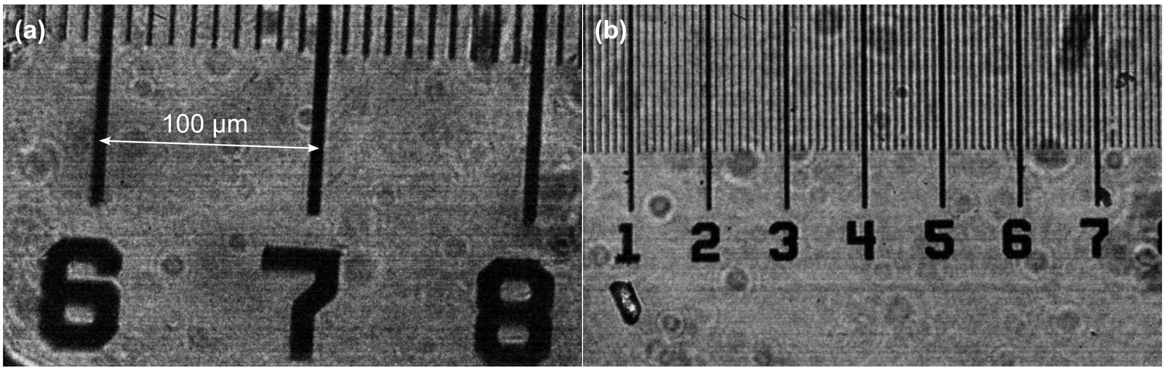

Figure A.1: Calibration of nanoCET. (a) Initial calibration using small-f lens. The distance between the large lines is 100 µm and between the small lines 10 µm. By measuring the distance in pixels between these lines, we can find the number of pixels that correspond to the known distance in µm. The calibration result is that 1 pixel corresponds to 0.139 µm. **(b)** Calibration of the setup using the lens with f=7.50 mm. The calibration gave that 1 pixel corresponds to 0.393 µm.

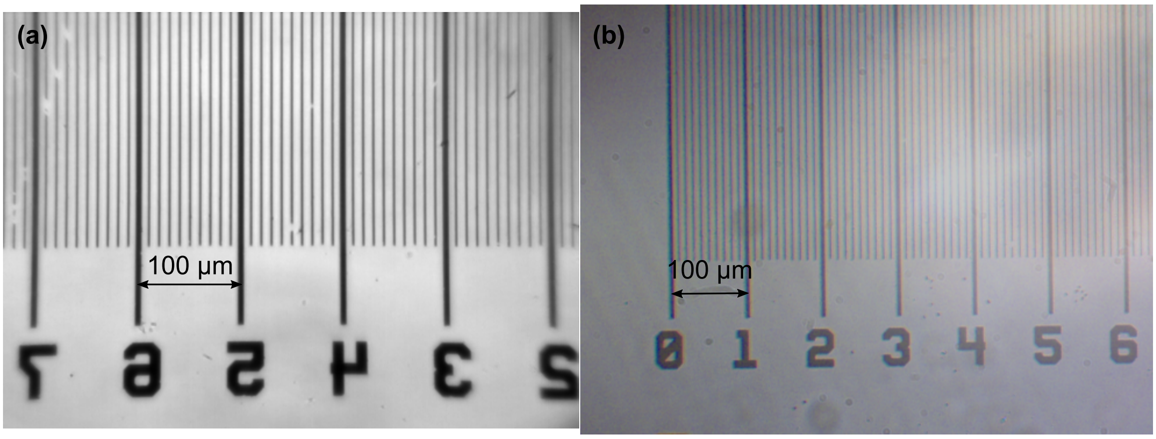

Figure A.2: Calibration images. **(a)** Calibration image for Hamamatsu camera. The calibration result is that 1 pixel corresponds to 0.620 µm. **(b)** Calibration image for the setup used for fiber characterization. The result of the calibration is that 1 pixel corresponds to 0.474 µm.

A.1.1. Increase of the FOV

We replaced the objective lens of the system with a lens with a larger focal length (f=7.50 mm) to decrease the magnification, and thus increase the FOV.

Figure A.1(b) shows one of the images of the micro-ruler obtained using the setup with the new objective lens. For the new system, the calibration gave that 1 pixel in the images corresponds to 0.393 µm. Therefore, the FOV is 755 µm × 472 µm.

A.2. Calibration of camera used for fluorescence detection

For the calibration of the camera (Hamamatsu ORCA-Flash4.0) used for the fluorescence detection, we used again the micro-ruler. By illumination with white light, we obtained the image of Figure A.2(a). We measured the distance between the large lines of the micro-ruler in pixels, and then knowing that this distance is 100 µm, we calculated the distance which corresponds to 1 pixel. The result is that 1 pixel corresponds to 0.620 µm.

A.3. Calibration of setup used for fiber characterization

To calibrate the setup that we used for the characterization of the pulled optical fibers (Figure 4.3(a)), we used again the micro-ruler and white light illumination. Figure A.2(b) shows an image of the micro-ruler. Using this image, the calibration gave that 1 pixel corresponds to 0.474 µm.

Appendix B

Fiber alignment and light coupling into fiber core

This appendix provides a protocol for the fiber alignment and light coupling into the fiber core using the nanoCET setup and the DisperFluo software of Dispertech*.

B.1. Fiber alignment

The first step needed to perform measurements is to align the multi-mode optical fiber. The procedure of the fiber alignment is performed using the Fiber Alignment window of Disper Fluo software. The steps for the procedure of fiber alignment are the following:

1. Turn on the red LED (the button for the red LED is in the Microscope Alignment window).
2. Set the gain to zero.
3. Increase the exposure time to the required level to be able to see the surface of the fiber end on the camera (usually an exposure time around 150000-200000 µs is sufficient).
4. Move the piezo stage of the lens to focus the image. The speed of the piezo stage of the lens is controlled from the Microscope Alignment window and by pressing the '+' and '-' buttons we can move the lens.

   When the fiber end is in focus, we observe its surface on the camera (we observe an inner circle which is the fiber core, and an outer circle which is the cladding).
5. We can save the data with the 'Save core' button (the data are saved as a numpy array).

B.2. Light coupling into fiber core

After the fiber alignment, the next step is to couple the laser beam into the fiber core. The steps for the light coupling procedure are the following:

1. Turn on the laser from the Microscope Alignment window by setting its power at 3 (typically 3 is sufficient).
2. Decrease the exposure time to 10 µs.
3. Move the laser beam at the center of the core by moving the mirror which is placed on a piezo stage. The speed of the piezo stage of the mirror is controlled by the Fiber Alignment window.
4. When the laser spot is at the center of the core, we can focus using again the lens. The ideal case is to have a small, sharp, bright spot such as in Figure 5.1(b) (vi).

---

*Dispertech: `https://dispertech.com/home`

Appendix C

Scattering microscopy measurements

This appendix presents the initial results that we obtained for particle tracking using scattering microscopy measurements. The data used here are the same as the data of chapter 5. The initial analysis presented in this appendix uses a roughly estimated PSF size as input for the diameter parameter of TrackPy. This PSF size was estimated by eye. To optimize our results, we determined with an accurate way the PSF size as explained in 5.4.1, and the results are presented in chapter 5.

C.1. Parameters for tracking algorithm

The PSF size was estimated roughly by looking at the image of a particle and counting the pixels corresponding to the PSF width. The found diameter with this approach was 7 pixels. Using this diameter, the number of detected features over 100 frames was measured by the tracking algorithm for different values of the minimum mass (Figure C.1(a)). From the plot, we can see that for values of the minimum mass smaller than 120 the algorithm starts to detect particles. For small values of the minimum mass (< 5) the number of detected features sharply increases and probably many of the detected features correspond to false-detected particles. The threshold that we initially selected was 25 which is maybe a bit larger than the lowest possible threshold.

C.2. Particle tracking results

After determining the parameters for the tracking algorithm, the particles in every frame were located and their positions were linked to create their trajectories. Figure C.1(b) shows the particle trajectories in 2 dimensions. Using the parameters of diameter d=7 pixels and minimum mass=25, the number of tracked particles was 876. The longest trajectory found is 339 frames which corresponds to approximately 4 seconds.

The hydrodynamic diameter distribution was calculated as explained in 5.5.2 and is illustrated in Figure C.1(c). The size distribution was fitted with an inverse Gaussian distribution and the calculated median diameter is d = 0.12 µm. The standard deviation of the distribution is 0.34 µm.

The hydrodynamic diameter of the particles was also calculated using the MSD of the ensemble of particles. By performing a linear fitting to the MSD it was possible to calculate the diffusion coefficient and the particle size (Figure C.1(d)). The found particle diameter using this approach is d = 0.48 ± 0.08 µm.

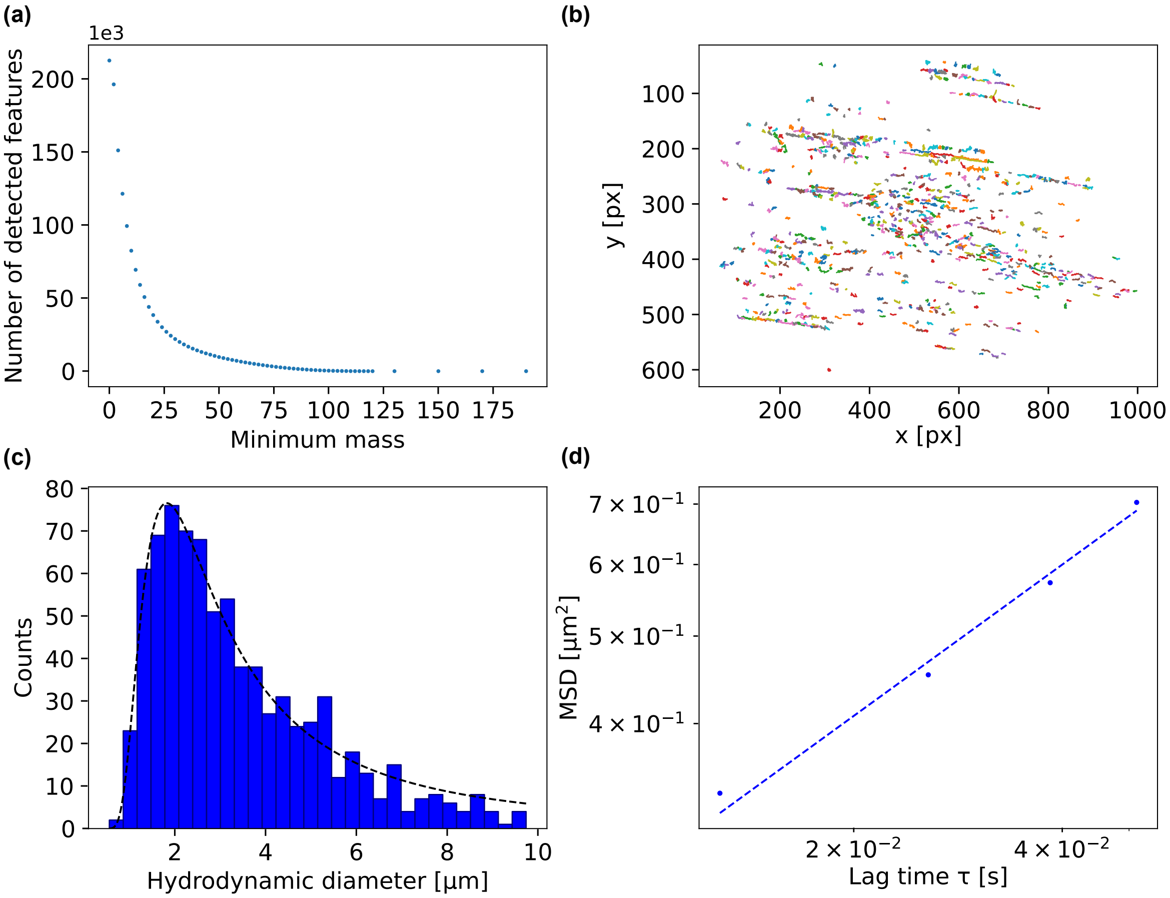

Figure C.1: Particle tracking using d=7. **(a)** Number of the found features over 100 frames as a function of the minimum mass. The diameter parameter has a value of 7 pixels. **(b)** Particle trajectories in 2 dimensions. The tracked particles are 876. **(c)** Distribution of the hydrodynamic diameter. The dashed line corresponds to an inverse Gaussian fitting. **(d)** MSD of the ensemble of particles fitted by a linear relation (dashed line).

Appendix D

Sample holder prototype: Design and fabrication process

A part of this project was the fabrication of a sample holder for the optofluidic chip. In the following sections, the design and fabrication process of the sample holder are explained.

D.1. Sample holder design

The requirements for the design of the sample holder are: (a) to be compatible with the design of the optofluidic chip, and (b) to be compatible with the experimental setup.

The optofluidic chip consists of a pulled optical fiber integrated with a flow cell. Thus, the sample holder needs to have a part with the size and thickness of the flow cell and a groove where the fiber can fit. Moreover, it is important to have a stable configuration, so we stabilize the chip position using magnets, and the fiber position using a fiber clamp (Figure D.1(a)).

Regarding the experimental setup, the available space for the sample holder implies some restrictions in the design. We chose the sample to be placed along the y direction due to the limited space in the x direction. Additionally, the objective lens in the experimental setup

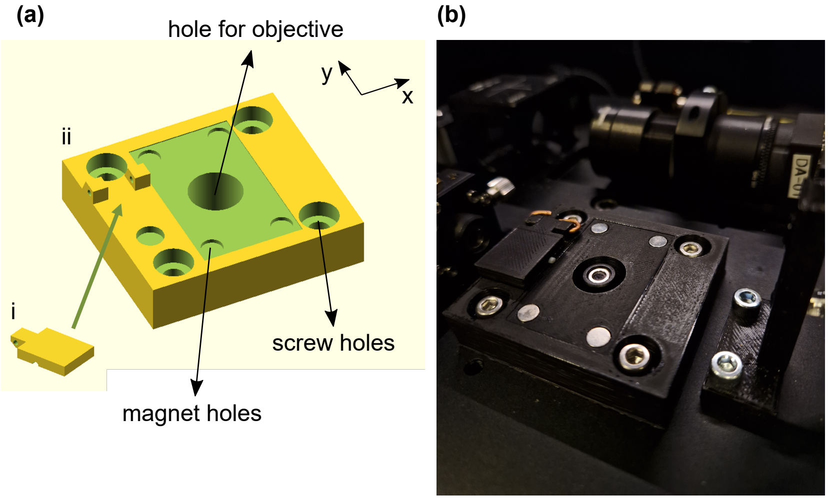

Figure D.1: Sample holder design. (a) 3D design of the sample holder which consists of two parts: (i) the fiber clamp, and (ii) the main part of the sample holder. The 3D structures were designed in OpenSCAT software. The design includes holes for the screws that will be used to mount the holder in the experimental setup, holes for the magnets that we use to increase the sample stability, and a hole for the objective lens. **(b)** Image of the 3D printed sample holder placed in the experimental setup.

has a fixed position, and the sample needs to be at the center of the objective.

D.2. Fabrication process

The sample holder was fabricated using filament 3D printing. We performed trials to find the ideal combination of 3D printing settings to achieve the desired structure. The most important features of the structure are to have a smooth top surface and robustness.

3D printing involves many challenges that we had to deal with during the sample holder fabrication. One of the most common challenges is the shrinking of the plastic material used, due to the high temperature during the printing procedure. This makes challenging the achievement of the desired sizes of the different parts of the 3D printed object. Therefore, it is important to take the shrinking of the material into consideration when choosing the dimensions of the structure components.

D.2.1. 3D printing steps

For the filament 3D printing we used the Original Prusa i3 MK3S printer and the PrusaSlicer software[*]. The steps for the 3D printing procedure are the following:

1. Import the design files (STL file format) in PrusaSlicer software.
2. Select the printing settings.
3. Slice the object.
4. Export the file on the SD card of the 3D printer.
5. Import the SD card on the printer and choose the file.

D.2.2. 3D printing settings

In this section an overview of the settings that we used to 3D print the sample holder is given.

General settings:

- Filament: PLA
- Printer: 0.4 mm nozzle
- Infill: 60%
- Enabled brim option

In PrusaSlicer software there are also more advanced print settings and filament settings. Table D.1 summarizes the settings that we used for the fiber clamp (part (i) in Figure D.1(a)), and the sample holder printing (part (ii) in Figure D.1(a)). Below, an explanation of the different parameters is provided.

Perimeters:
Perimeters define the minimum number of outlines forming the object wall. The number of perimeters is the most important parameter for the strength of the printed object. The default minimum number of perimeters is 2, but we increased that to 3 to increase the strength of the structure.

---

[*] PrusaSlicer: `https://prusa3d.com`

Infill:
Fill density does not significantly affect the strength of the structure, but is related to the compression resistance of the object. For our structure, we chose a high fill density (60%) to increase the compression resistance since we want to use screws to mount the sample holder in the experimental setup. The fill pattern that we used was cubic.

Ironing:
The ironing option is used when is important to have a smooth top surface. When ironing is enabled, the hot nozzle moves over the top layer of the object after printing and it flattens the plastic material in the top layer. Also, the nozzle extrudes a tiny amount of filament while moving over the top layer, and thus is possible to fill in any gaps in the top layer.

The flow rate of ironing defines the percentage of the material that is extruded from the nozzle during ironing. The default value for the flow rate is 15%. We reduced the flow rate to 10% for the 3D printing of the fiber clamp and to 5% for the sample holder. Reduction of the flow rate means that less material is extruded from the nozzle and this can help to avoid some negative results of the ironing option, such as not sharp features of the printed object.

Brim:
The brim is an outline around the object that we want to print which increases the surface area of the first layer. This leads to a better adhesion of the object to the bed of the printer. In general, a brim width of at least 3 mm is used. For our case, we selected a brim width of 5 mm to ensure that our structure would adhere properly to the bed during the whole 3D printing procedure.

Bed temperature:
The default temperature of the bed is 60 °C. For the layers of the sample holder, we increased the bed temperature to 65 °C to increase the adhesion of the object. We decided to do that because we performed a 3D printing trial where the sample holder was detached from the bed during printing.

An additional setting that we used, is the variable layer height which enables 3D printing of thick layers when a layer has a simple structure, and printing of thinner layers for layers with a more detailed structure.

The 3D-printed sample holder was used as a prototype to fabricate an aluminium sample holder that was used for the experiments of this project.

3D printing settings		
Print settings	**Fiber clamp**	**Sample holder**
Layers and perimeters:		
Perimeters:	3	3
Infill:		
Infill:		
○ Fill density:	60%	60%
○ Fill pattern:	cubic	cubic
Ironing:		
○ Enable ironing:	yes	yes
○ Flow rate:	10%	5%
Skirt and brim:		
Brim width:	5 mm	5 mm
Filament settings		
Temperature:		
Bed:		
○ First layer:	60 °C (default)	60 °C (default)
○ Other layers:	60 °C (default)	65 °C

Table D.1: 3D printing settings

Appendix E

3D printing of holder and mask for fiber alignment

For the fabrication of the optofluidic chip, it was necessary to place the tapered optical fiber at the correct position on the bottom glass slide. For this purpose, we designed and 3d printed holder to place in the bottom glass slide, and a mask to place on top of the glass slide. The mask has a slit where the fiber can be placed to be at the desired position on the glass slide. Figure E.1 shows the 3D designs of the holder and the mask.

For the 3D printing, we used the Original Prusa i3 MK3S printer and the PrusaSlicer software as for the sample holder. The settings that we used are given below.

General settings:

- Filament: PLA
- Printer: 0.4 mm nozzle for the holder and 0.25 mm nozzle for the mask
- Infill: 20%
- Enabled brim option

To 3D print the mask we used some additional settings to achieve the correct thickness for the slit. We selected to print first the external perimeters, and we set the extrusion multiplier for the filament to 0.98. This means that the amount of filament extruded is 98% and not 100% which is the default.

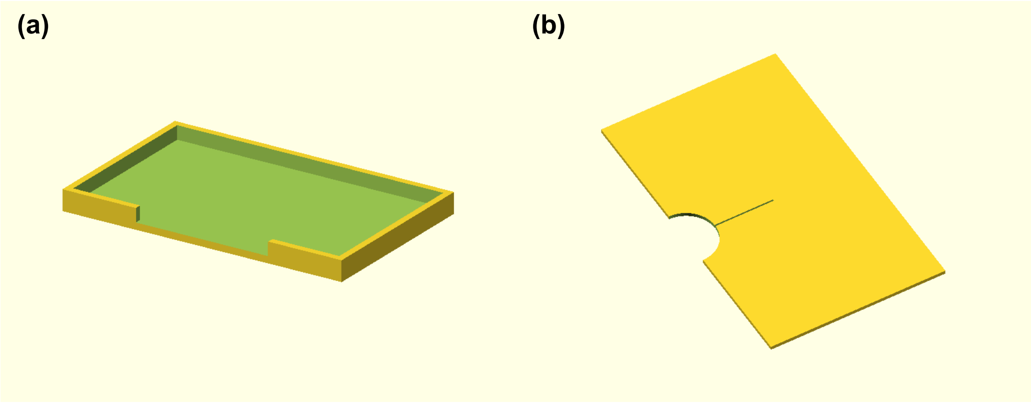

Figure E.1: Holder and mask for fiber alignment. (a) 3D design of the holder for the glass slide. **(b)** 3D design of the mask for fiber alignment. The mask has a slit with the fiber thickness and a semi-circular cut to stick the fiber on the glass slide before removing the mask. The 3D structures were designed in OpenSCAT software.